Solar Energy 155 (2017) 1462–1481

Contents lists available at ScienceDirect

Solar Energy

journal homepage: www.elsevier.com/locate/solener

Thermochemical H_2O and CO_2 splitting redox cycles in a $NiFe_2O_4$ structured redox reactor: Design, development and experiments in a high flux solar simulator

S. Lorentzou [a,*], D. Dimitrakis [a,b], A. Zygogianni [a], G. Karagiannakis [a], A.G. Konstandopoulos [a,b,*]

[a] Aerosol & Particle Technology Laboratory, Chem. Process & Energy Resources Inst., Center for Research & Techn.-Hellas (APTL/CPERI/CERTH), 6th klm. Charilaou-Thermi Rd, P.O. Box 361, 57001 Thessaloniki, Greece
[b] Aristotle Univ. of Thessaloniki, 54006, Univ. Campus, Thessaloniki, Greece

ARTICLE INFO

Article history:
Received 28 April 2017
Received in revised form 30 June 2017
Accepted 3 July 2017
Available online 19 September 2017

Keywords:
Redox thermochemical cycles
H_2O-CO_2 splitting
Structured reactors
Solar fuels

ABSTRACT

A high flux solar simulator allows the lab-scale assessment of solar reactor concepts by irradiating a target with high flux thermal energy, similarly to reactors installed in concentrated solar radiation facilities such as central towers with a heliostat field. In the current study, the design and construction of a high flux solar simulator facility for near realistic solar experiments is presented. A simple, cavity-tubular thermochemical reactor is employed for the evaluation of the redox activity of structured monolithic bodies (foams and honeycombs) consisting entirely of $NiFe_2O_4$ w.r.t·H_2O splitting, CO_2 splitting and combined H_2O-CO_2 splitting reactions. Experiments under realistic conditions, i.e. a solar reactor under irradiation, were conducted to assess the solar fuels production capability, which was examined at the structure level and the reactor level. The best performing structure was the $NiFe_2O_4$ foam. Further multilevel research (structure, reactor as well as redox material), will improve product yield and reactor efficiency.

1. Introduction

Solar energy is considered to be the only natural source, from the alternative energy sources, that is practically inexhaustible and can cover the energy demands at a global scale. A possible way to efficiently exploit the solar potential could be its transformation into energy carriers such as solar H_2 or solar fuels. To this respect, Concentrating Solar Thermal (CST) technologies can be employed for the implementation of thermochemical cycles using solar energyfor the production of H_2 or solar fuels by splitting H_2O or CO_2. In the last decades several thermochemical cycles for solar hydrogen and solar fuels production have been proposed (Funk, 2001; Carty et al., 1981; Mcquillan et al., 2010), reviewed and investigated (Kodama and Gokon, 2007; Steinfeld, 2005; Abanades et al., 2006; Perkins and Weimer, 2004). The two-step redox stoichiometric and non-stoichiometric cycles (Agrafiotis et al., 2015) of single or mixed metal oxides (e.g. zinc oxide, iron oxides, ferrites, ceria-based and perovskite compositions) have attracted the attention of the research community (Palumbo and Fletcher, 1988; Scheffe et al., 2010; McDaniel et al., 2013; Kuhn et al., 2013; Lorentzou et al., 2013; Lorentzou et al., 2015; Gokon et al., 2008; Loutzenhiser et al., 2010a; Furler et al., 2012; Chueh et al., 2010). The current work focuses on non-stoichiometric cycles for the production of H_2 and CO from the respective H_2O and CO_2 splitting. The general scheme can be written as:

$$M_{x1}N_{x2}O_y \leftrightarrows M_{x1}N_{x2}O_{y-\delta 1} + \delta_1/2O_2 \quad (1) \quad (\text{Temperature range} : 1100-1500\,^{\circ}C)$$

$$M_{x1}N_{x2}O_{y-\delta 1} + \delta_2 H_2O \rightleftarrows M_{x1}N_{x2}O_{y-\delta 1+\delta 2} + \delta_2 H_2 \quad (2) \quad (\text{Temperature range} : 800-1200\,^{\circ}C)$$

$$M_{x1}N_{x2}O_{y-\delta 1} + \delta_3 CO_2 \rightleftarrows M_{x1}N_{x2}O_{y-\delta 1+\delta 3} + \delta_3 CO \quad (3) \quad (\text{Temperature range} : 800 - 1200^{\circ}C)$$

where δ_1, δ_2, δ_3 represent oxygen deficiencies referring to the thermal reduction step (δ_1) and the material after oxidation by H_2O (δ_2) and CO_2 (δ_3) respectively; where M, N are metal/rare earth elements and $M_{x1}N_{x2}O_y$ is a ferrite/metal oxide/perovskite.

* Corresponding authors at: Aerosol & Particle Technology Laboratory, Chem. Process & Energy Resources Inst., Center for Research & Techn.-Hellas (APTL/CPERI/CERTH), 6th klm. Charilaou-Thermi Rd, P.O. Box 361, 57001 Thessaloniki, Greece (A.G. Konstandopoulos).

E-mail addresses: souzana@cperi.certh.gr (S. Lorentzou), agk@cperi.certh.gr (A.G. Konstandopoulos).

http://dx.doi.org/10.1016/j.solener.2017.07.001
0038-092X/

There are several solar reactor concepts that are investigated for the implementation of such cycles, which have been developed by research groups worldwide (Furler et al., 2012; Chueh et al., 2010; Agrafiotis et al., 2005; Furler et al., 2012; Roeb et al., 2011; Houaijia et al., 2013; Gokon et al., 2008; Gokon et al., 2009; Gokon et al., 2011; Miller et al., 2006; Miller et al., 2012; Loutzenhiser et al., 2010b; Haueter et al., 1999; Koepf et al., 2012; Gokon et al., 2011; Lichty et al., 2012) and were extensively reviewed in e.g. (Steinfeld, 2005; Agrafiotis et al., 2015; Konstandopoulos and Lorentzou, 2010; Alonso and Romero, 2015). A broad classification of the different reactor concepts is shown in the following Table 1.

The core of structured reactors (Agrafiotis et al., 2015; Furler et al., 2012; Chueh et al., 2010; Agrafiotis et al., 2005; Furler et al., 2012; Roeb et al., 2011; Houaijia et al., 2013; Gokon et al., 2008; Gokon et al., 2009; Gokon et al., 2011; Miller et al., 2006; Roeb et al., 2006; Säck et al., 2016; Kodama et al., 2008; Kawakami et al., 2014; Miller et al., 2008; Walker et al., 2012; Gokon et al., 2011), which is the interest of the current article, are monolithic structures (such as honeycomb monoliths or foams) that may consist either of inert substrates that are coated with the active redox material or they can be made entirely of the redox material. The latter have the benefit of avoiding undesirable interactions of the redox material with the substrate. However, the manufacturing of robust structures that are thermo-mechanically and chemically durable in the course of multiple cycles is challenging.

Another challenge is the evaluation of the candidate structures and reactor concepts under realistic conditions. Initially, the development of structured bodies is done at small scale and for their evaluation, laboratory test rigs are applied involving the use of electrical furnaces to achieve the required high temperatures. However, when it comes to the evaluation of the small scale subjects under realistic conditions or as assemblies into structured reactors then another approach is required that can simulate the solar conditions, namely a "solar simulator".

A solar simulator is a lab-scale device that enables the irradiation of targets with concentrated artificial light. This artificial light is created by lamps and is concentrated by reflectors that redirect it towards a common target. The scope of such an indoor facility is to simulate the directional, spatial and spectral distributions of concentrated solar radiation obtained at the focal plane of highly concentrating solar systems (i.e. parabolic dish, solar tower, solar furnace). Comparatively to these large infrastructures, solar simulators have a low cost and allow the controlled, high temperature experimental conditions avoiding geographical challenges or the intermittent nature of the concentration of sunlight.

With a spectrum that closely matches that of the sun, a solar simulator facility is a "sun-in-a-box", an always available lab-scale, highly adjustable device that provides concentrated radiation. Solar simulators are mainly employed for testing components, materials and reactors for high temperature thermal and thermochemical applications such as redox cycles for solar fuels research. Several of these high power and high flux solar simulators for high temperature solar thermochemical experiments exist worldwide (Kuhn and Hunt, 1991; Jaworske et al., 1996; Hirsch et al., 2003; Guesdon et al., 2006; Petrasch et al., 2006; Codd et al., 2010; Alxneit and Dibowski, 2011; Krueger et al., 2011; Erickson, 2012; Nakakura et al., 2015; Li et al., 2014; Dimitrakis et al., 2013; Sarwar et al., 2014; Wang et al., 2014; Levêque et al., 2016; http://www.dlr.de/dlr/en/desktopdefault.aspx/tabid-10202/334_read-21807/#/gallery/26638/, 2017). An overview of existing high power solar simulators is presented in Table 2.

As mentioned earlier, solar simulators can be employed for the evaluation of different materials and solar reactor designs for solar redox thermochemical applications prior to their integration in actual solar facilities.

Indicatively, some representative studies that have been conducted for the evaluation of redox structures with respect to H_2O and CO_2 splitting are (Gokon et al., 2009; Gokon et al., 2011; Kawakami et al., 2014) for the case of ferrite coated foam structures and (Furler et al., 2012; Chueh et al., 2010) for CeO_2 foams. More specifically for H_2O splitting in Gokon et al. (2009) it was reported that the maximum rate of H_2 production was approximately 5 μmole/min/g_{device} (device: $NiFe_2O_4$ coated foam), while in Kawakami et al. (2014) the maximum rate measured for the best ferrite foam was 0.1 ml/min/g_{device}. In (Gokon et al., 2011) the total production of H_2 varied from 1.1 to 4.6 ml/g_{device}. In (Chueh et al., 2010) approximately 4.6 ml/g_{CeO2} have been reported as a total H_2 yield corresponding to one H_2O splitting cycle for the CeO_2 foam.

In the case of CO_2 splitting, investigations on structured monolithic bodies were conducted on CeO_2 foam structures. In (Furler et al., 2012) total CO yields of 1.465–5.69 ml/g_{CeO2} were reported for CeO_2 foam assemblies that were previously regenerated at temperatures ranging from 1420 to 1600 °C respectively.

Finally, in the case of simultaneous introduction of H_2O and CO_2 for the production of syngas on a CeO_2 felt, it has been reported in Furler et al. (2012) a total yield of H_2 and CO of approximately 2.21 ml/g_{CeO2} and 0.94 ml/g_{CeO2} respectively. No H_2O-CO_2 co-feeding experiments have been reported for CeO_2 foam structures.

The study presented in this article is a comprehensive work covering all stages from material, to structures manufacturing, to reactor integration with a radiation concentration facility in the scope of concentrating solar technologies. More specifically, in the next paragraphs, the most important components of a dual foci solar simulator facility are described, in terms of design and manufacturing. The subsequent integration of an indirectly heated solar reactor with the solar simulator facility is discussed. The study presents realistic results on the evaluation of novel structured bodies consisting entirely of the active redox material ($NiFe_2O_4$) with respect to solar-thermochemical H_2O and CO_2 splitting reactions.

2. Solar simulator

2.1. Design principles

The general characteristics of high temperature solar concentrators (tower, parabolic dish, etc.), that should be reproduced in a solar simulator, include the beam geometry, the irradiated area, the relative distribution of flux and solar spectral distribution. An equally important design factor is the targeted thermal power that will reach the receiver. A delivered power of 10–12 kW_{th} to the receiver is considered a safe target for most high temperature lab-scale solar chemistry experiments and this power should in general be considered over a 60 mm diameter hot-spot. Additionally, a solar simulator must offer the option to vary the power intensity, the spot size and uniformity of radiation distribution. Lastly, several physical and practical limitations have to be

Table 1
Different solar reactor concepts.

Solar reactor concept	Heat transfer mechanism	Reactor main components	Operation principle
	Directly irradiated	Particles	Moving receiver
	Indirectly irradiated	Structured bodies	Non-moving receiver

Table 2
Overview of existing solar simulators.

Solar simulator	Characteristics		Ref.
PSI	Single 20–30 kW_{el} Xenon arc lamp Aluminum ellipsoid reactors Peak flux of 16000 kW_{th}/m^2 Power of 3 kW_{th} over a 7 × 7 cm area	(1991)	Kuhn and Hunt (1991)
NASA	Nine 30 kW_{el} Xenon arc lamps Nearly elliptical vapor deposited aluminum reactors with SiO_2 protective coating Peak flux of 1.7 kW_{th}/m^2 Power of 19.7 kW_{th} over 158 cm radius area Ellipsoidal aluminum reactors (three pieces, diamond machined inner surfaces) Peak flux of 1300 kW_{th}/m^2	(1996)	Jaworske et al. (1996)
PSI	Single 1 kW_{el} Xenon arc lamp	(2006)	Guesdon et al. (2006)
PSI	Ten 15 kW_{el} Xenon arc lamps Ellipsoidal aluminum reactors, highly polished three-layered: primer, vapor deposited Aluminum, protective SiO_2 Peak flux of 11000 kW_{th}/m^2 Power of 20 kW_{th} on a 60 mm diameter target	(2007)	Petrasch et al. (2006)
MIT	Seven 1.5kW_{el} metal halide lamps NEMA standardized spun-Aluminum ellipsoidal reactors with secondary concentrator Peak flux of 60 kW_{th}/m^2 Average flux of 45 kW_{th}/m^2 on a 38 cm diameter area	(2010)	Codd et al., (2010)
DLR	Ten 6kW_{el} Xenon arc lamps Aluminum ellipsoid reactors, polished and coated Peak flux of 4000 kW/m^2 11 kW_{th} over a 140 × 140 mm^2 area (distributed spots)	(2011)	Alxneit and Dibowski (2011)
Un. of Minnesota	Seven 6.5 kW_{el} Xenon arc lamps Spun Aluminum ellipsoid reactors, polished and coated with quartz Peak flux of 3700 kW/m^2 7.5 kW_{th} over a 60 mm diameter area	(2012)	Krueger et al. (2011)
University of Florida	Seven 6 kW_{el} Xenon arc lamps Peak flux of 4230 kW/m^2	(2012)	Erickson (2012)
Niigata University	Nineteen 7 kW Xenon arc lamps Peak flux over 3000 kW_{th}/m^2 33.3 kW_{th} over a 200 mm diameter area	(2013)	Nakakura et al. (2015)
IMDEA	Seven 6 kW_{el} Xenon arc lamps Ellipsoid reactors coated with Aluminum and protective polymer Peak flux of 3800 kW_{th}/m^2 5.3 kW_{th} over a 60 mm diameter area	(2013)	Li et al. (2014)
APTL	Eleven 6 kW_{el} Xenon arc lamps Peak flux of 4800 kW_{th}/m^2 18 kW_{th} over a 60 mm diameter area	(2013)	Dimitrakis et al. (2013)
HFSS-SERL	Single 7 kW_{el} Xenon arc lamps Ellipsoid reactor Peak flux of 3583 kW_{th}/m^2 Power of 0.96 kW_{th} over a 70 mm diameter area	(2014)	Sarwar et al. (2014)
KTH	Twelve 7 kW_{el} Xenon arc lamps Fresnel lens concentrators Peak flux of 6700 kW/m^2 19.7 kW over 200 mm diameter area	(2015)	Wang et al. (2014)
EPFL	Eighteen 2.5 kW_{el} Xenon arc lamps Peak flux 21700 kW/m^2 Average flux 3.8 MW/m^2 over a 50 mm diameter area.		Levêque et al. (2016)
DLR-Jülich	149 individually adjustable Xenon short-arc lamps. Peak flux 11 MW/m^2	(2017)	http://www.dlr.de/dlr/en/desktopdefault.aspx/tabid-10202/334_read-21807/#/gallery/26638/(2017)

considered as well, such as available room length and height, lamp operation requirements, safety clearances and others. A unique design point of the solar simulator that is described in the current work, is the capability of the simultaneous irradiation of two distinct targets. Switching from single focus to dual foci takes place in an easy and user friendly way without needing to refocus each unit.

The solar simulator is separated in blocks (lamp blocks) (see Fig. 1) with main subcomponents being: (i) the lamp, (ii) the reflector, (iii) the positioning mechanism for each lamp (using this 3-axes positioning mechanism the lamp can slide in and out of the reflector focus), (iv) the lamp's blower, (v) temperature sensors for reflector temperature measurement and a differential pressure sensor for fan monitoring (vi) the igniter, (vii) the microcontroller running in-house developed software for controlling the subcomponents of the unit and for communication of each lamp unit to the respective rectifier and to the network.

Considering the spectral requirements, the lamp type of choice is the Xenon Short Arc Lamps. Such lamps have an emission spectrum that closely matches that of sunlight (OSRAM, 2008). The

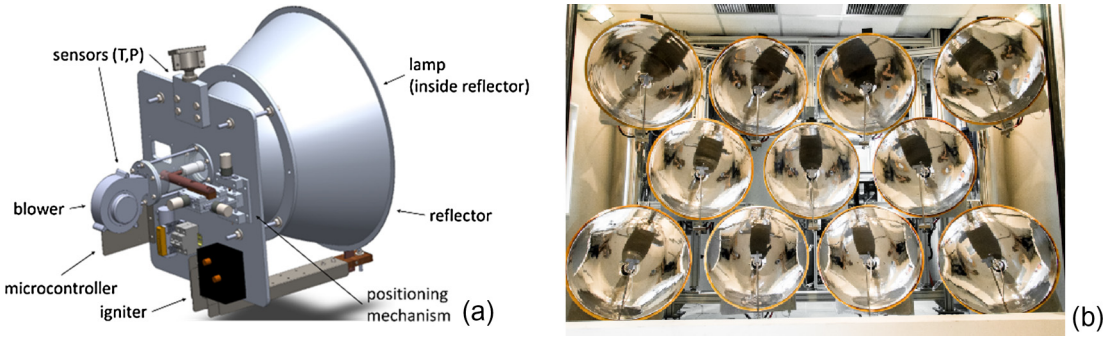

Fig. 1. (a) Lamp block with subcomponents, (b) high flux solar simulator front.

lamp power and hot restart ability are of great importance. Based on previous relevant work (Petrasch et al., 2006; Alxneit and Dibowski, 2011; Krueger et al., 2011; Erickson, 2012), the most practical option was considered to be a forced convection cooled 6 kW_{el} lamp (OSRAM XBO 6000W/HSLA OFR). The number of lamps that were used was determined by (conservative) estimations as presented in Table 3.

Considering the estimations presented in Table 3 the required electrical power is in the order of 54–66 kW_{el}, or 9–11 lamps of 6 kW_{el} power each for two focal points (see Fig. 2).

The supporting structure accommodates 11 units in a hemispherical configuration and easy switching to dual targets to achieve the dual foci. The chosen configuration consists of two arrays in the shape of an X, each with 5 units and its own focus, that can be slightly rotated with respect to the central axis of symmetry of the solar simulator to also allow the irradiation of a single common focus. The 11th unit is fixed among these arrays along the axis symmetry and is stationary. This configuration was termed 2X + 1. Each X array rests on bearings that allow for the manual rotation to the secondary target.

Each ray originating from one focus of an ellipse that is reflected upon its circumference will pass through the second focus. This ability renders it the ideal geometric shape for ellipsoid reflectors with a light source at the first focus and a target at the second. The design equation of an ellipse in Cartesian coordinates is given as:

$$\frac{x^2}{\alpha^2}+\frac{y^2}{b^2}=1 \tag{1}$$

where a is the semi-major axis and b is the semi-minor axis. Additionally f is the focal distance, defined as:

$$f^2=\alpha^2-b^2 \tag{2}$$

c is the semi-focal distance defined as:

$$c=\frac{f}{2} \tag{3}$$

and ε is the eccentricity defined as:

$$\varepsilon=\frac{c}{\alpha} \tag{4}$$

The reflectors are truncated ellipsoids of revolution. The parameters (Fig. 3b) that have to be considered and the governing equations in order to design such a reflector are reported in detail in Petrasch et al. (2006) and are: d_t is the truncation diameter of the ellipsoid, a_t is the truncation angle and h is the height (or depth) of the ellipsoid.

The equations that express the ellipse parameters a and b in terms of c, a_t and d_t are (from Petrasch et al. (2006)):

$$\alpha^2=\mu+c^2 \tag{5}$$

$$b^2=\mu \tag{6}$$

$$\mu=\frac{f(1/2)d_t^2(1+\tan^2\alpha_t)+d_t(-2c\tan\alpha_t+\xi)}{2} \tag{7}$$

$$\xi=\sqrt{(1+\tan^2\alpha_t)[(d_t^2/4)(1+\tan^2\alpha_t)-2cd_t\tan\alpha_t+4c^2\tan^2\alpha_t]} \tag{8}$$

Table 3
Estimated efficiencies for the definition of the number of lamps required.

	Factor	Power
Lamp nominal electrical power	–	6.00 kW_{el}
Electric to radiative energy conversion	≈50% (Alxneit and Dibowski, 2011)	3.00 kW_{th}
Reflectivity of aluminum ellipsoid	90%	2.70 kW_{th}
Errors of ellipsoid geometry	20%	2.16 kW_{th}
Thermal power per target	–	10–12 kW_{th}
Number of lamps needed	–	9–11

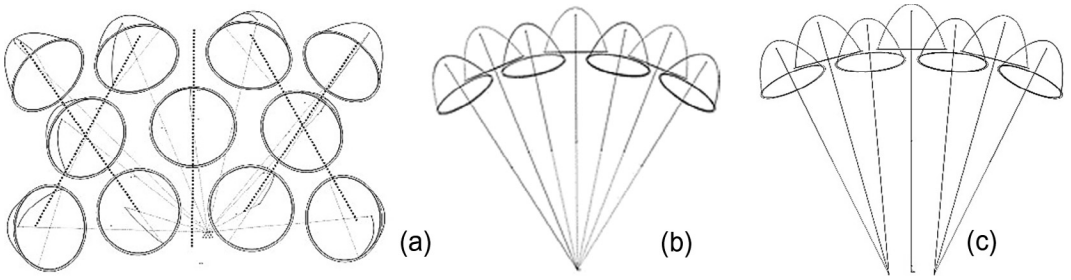

Fig. 2. (a) two arrays of 5 units plus an additional in a 2X + 1 configuration, that have (b) a common focus and (c) can slightly rotate to change their (common of 5) focus.

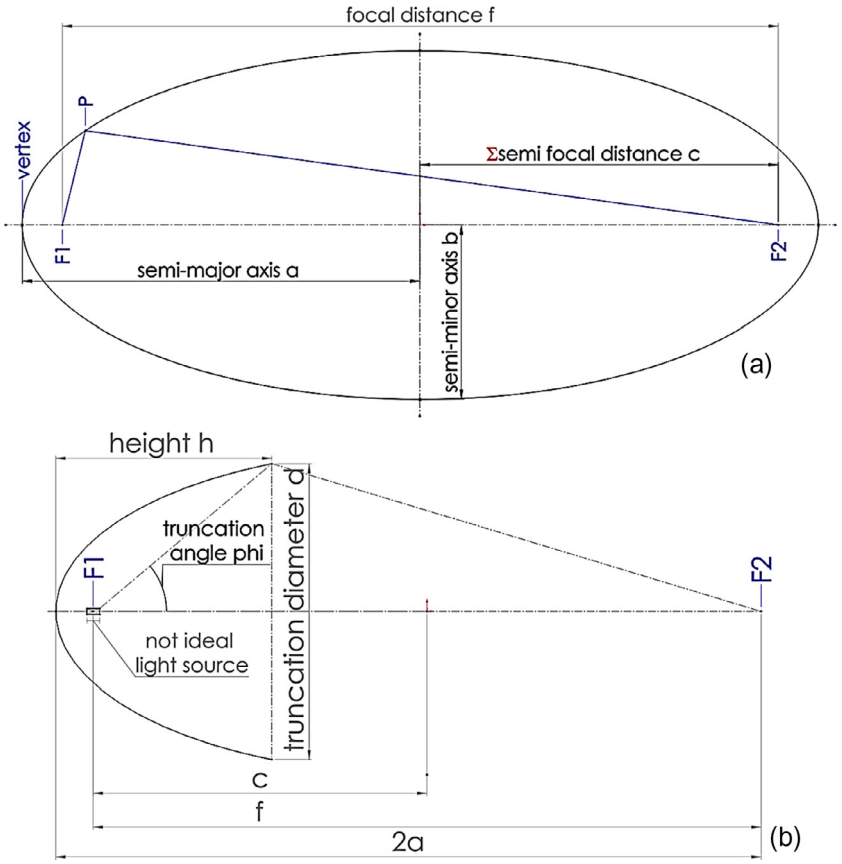

Fig. 3. Design parameters of (a) an ellipse and (b) a truncated ellipsoid.

The assumptions of the design strategy followed, in order to obtain the optimum reflectors include the following points:

The maximum possible truncation diameter is defined. The larger the truncation diameter, the higher the reflected fraction of radiation emitted from the source. The practical restrictions imposed to the maximum truncation diameter are: the manufacturing technique and the available height of the installation site.

The minimum possible focal length is determined. Smaller focal lengths lead to minimization of specular errors. The minimum achievable focal length depends on the number of units. and the configuration selected (optical clearance and rim angle of 35–45°) as well as practicality and safety reasons (enough space for safety and control mechanisms e.g. bay door, adequate space for a technician to safely install a unit or a reactor).

Having the truncation diameter and focal length set, the value of the truncation angle is varied. Using Eqs. (5)–(8), and varying the value of the truncation angle, different reflectors are calculated with varying transfer efficiencies. The transfer efficiency is defined as the fraction of radiation reaching the target to the radiation leaving the source (Petrasch et al., 2006):

$$n = \frac{P_{target}}{P_{source}} \tag{9}$$

The optimum reflectors have a maximum transfer efficiency. The transfer efficiency is calculated using ray tracing runs.

Based on the anticipated requirements imposed by the reflector size, the manufacturing technique selected was metal spinning of a 2.5 mm thick aluminum sheet. The formed aluminum reflector, was then thoroughly polished, coated with a thin film of aluminum to increase reflectivity and top coated with a SiO_2 protective layer to avoid oxidation of the aluminum coating.

The available total height of the solar simulator installation is 3000 mm where 150 mm must be left free from the bottom reflector for practical reasons (installation of the unit) and 350 mm from the top reflector (300 mm air ducts must pass over the array of units). That leaves a net height of 2500 mm available for the reflectors. Considering a square footprint for each reflector in the X configuration and allowing for a safety distance among neighbouring reflectors of 100 mm, the maximum possible truncation diameter is set at 735 mm (Fig. 4a). Given the 2X + 1 configuration, the installation site limitations (room length) and other safety and practicality conditions, the minimum achievable focal distance is set at 3000 mm (Fig. 4b). For the ray tracing runs and the calculation of the transfer efficiency, the radiative power reaching a 100 mm × 100 mm target is divided by the fixed power emitted by the source as defined in Table 4 (see Fig. 5).

The source shape is approximated by a diffusively emitting sphere with an arc equal to the half width of the luminous area of the lamp as defined in the lamp datasheet (OSRAM, 2006). The light originating from the sphere is obstructed by the two electrodes to produce a spatial distribution as given in the lamp manual (OSRAM, 2008).

For each ray tracing calculation 10^6 rays are used, each reflector is considered to be a perfect mirror (100% reflectivity) while the electrodes and target are perfect absorbers. The results of the transfer efficiency calculations are presented in Table 4.

The optimum reflector dimensions must as well satisfy the following additional restrictions when assembled in the 2X + 1 configuration: (i) rim angle of the array must be between 35 and 45°, (ii) maximum tilt angle of lamp in horizontal operation should not exceed 15° (OSRAM, 2008), (iii) distance of lamp arc to ellipsoid vertex should exceed 80 mm to avoid high thermal stresses on the reflector (Alxneit and Dibowski, 2011).

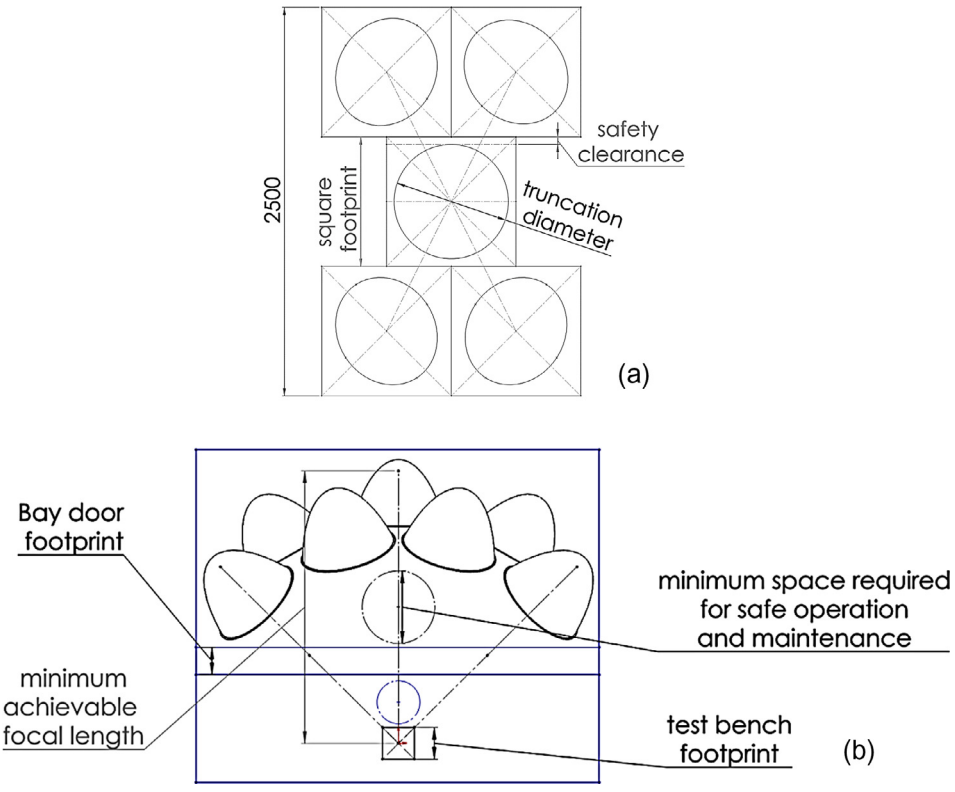

Fig. 4. (a) front footprint-maximum truncation diameter selection and (b) top footprint –minimum focal distance selection.

Table 4
Overview of reflector calculations: Ellipsoid and ray tracing.

	Ellipsoid calculations					
Fixed parameters						
Focal distance (m)	2c			3		
Truncation diameter (m)	d_{tr}			0.735		
	Varying parameter					
Truncation angle (°)	a_{tr}	35	45	55	65	75
	Ellipsoid parameters					
Reflector No.		R1	R2	R3	R4	R5
	ξ	2.14	3.89	6.89	14.47	42.17
	μ	0.22	0.28	0.34	0.40	0.48
Semi-major axis (m)	a	1.57	1.59	1.61	1.63	1.65
Semi-minor axis (m)	b	0.47	0.53	0.58	0.64	0.69
Length (m)	h	0.60	0.45	0.37	0.30	0.25
Eccentricity	ε	0.95	0.94	0.93	0.92	0.91
	Ray tracing calculations (power)					
Absorbed/emitted	n	0.680	0.735	0.728	0.666	0.565

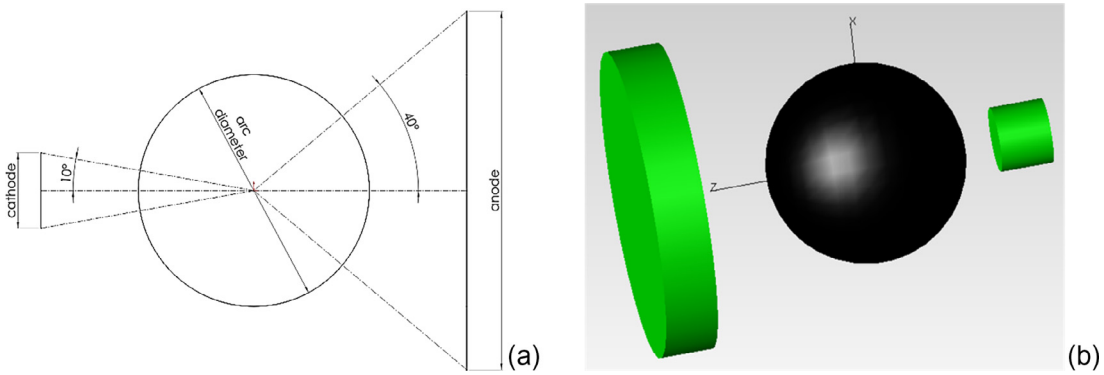

Fig. 5. Approximations of lamp source for raytracing calculations (a) schematic of source and electrodes, (b) 3D model of source.

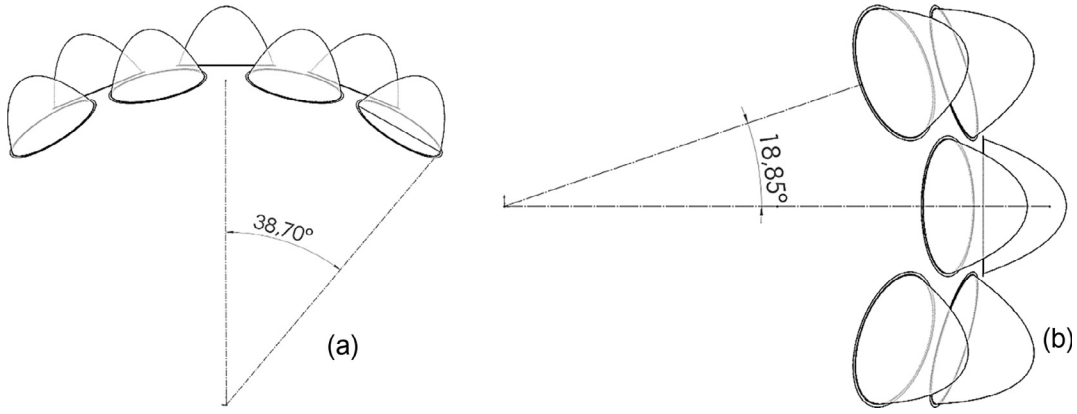

Fig. 6. Rim angle of Reflector 2 in the 2X + 1 configuration (a, top view) and tilt angle of Reflector 2 in the 2X + 1 configuration (b, right view).

As shown in Fig. 6, the selected reflector configured in the 2X + 1 satisfies conditions (i) and (ii) while for condition (iii) exceeds the maximum value by 25%. The latter is accepted, since it affects the arc stability, a parameter which is important for imaging applications but of less significance for the current experimental applications with concentrated artificial light. The final dimensions of the manufactured reflector are shown in Fig.7.

The enclosure of the solar simulator has to be light- and radiation proof, accommodate the safety measures and provide the required cooling to the lamps, the reflectors and the rest of the machinery installed in the assembly. The control station is located outside of the enclosure and allows the operation of both solar simulator and reactor and the safe monitoring via cameras and windows which may be opened during operation under certain conditions.

Each Lamp block forms a separate node of the Solar Simulator computer control network. There are twelve nodes in total, one for each Lamp Block and one for the cooling unit (a). The microprocessor attached on each node is responsible for the communication of the node with the network master controller, which is a PLC hosted in the main electrical cabinet. User access to the PLC master controller is provided by an industrial grade PC which enables the operation and control of the Solar Simulator through a user friendly interface (Fig. 8b).

To accurately adjust the focus of the lamps of the solar simulator, the main criterion is the hot spot size. Ideally it should be equal to the theoretical spot calculated by the ray tracing analysis. The hot spot size was determined with the help of a high quality CCD monochrome camera, with chip dimensions: 4.8 mm × 6.4 mm (height × width), equipped with a 75 mm focal length zooming lens and the appropriate UV and optical filters that reduce the spot brightness. On the left side of Fig. 9 the heat flux distribution on a 200 mm × 200 mm metallic absorber is depicted using ray tracing software.

The light source is considered as above, while the reflector reflectivity is set at 90%. The right side image of Fig. 9, depicts the actual image of the metallic target during the lamp operation. The object height with this equipment is calculated to be 190 mm (top and bottom lines in Fig. 9). There is a good agreement between the hot spot of the theoretical approach (on the left of Fig. 9) and the experimental image (on the right of Fig. 9).

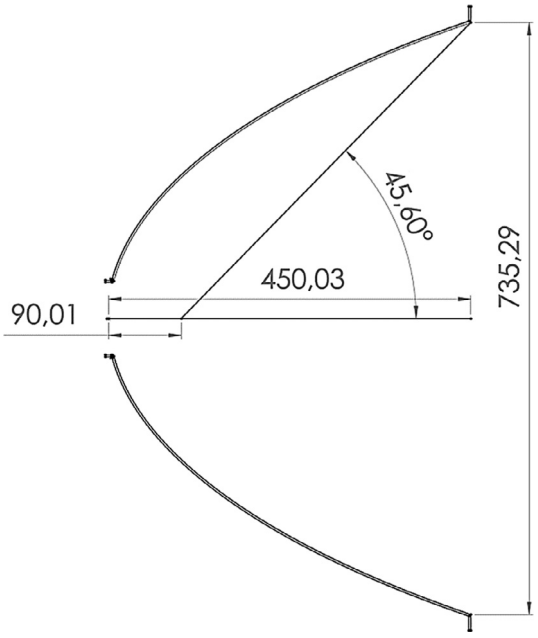

Fig. 7. Drawing of the ellipsoidal aluminum reflector for manufacture by metal spinning.

3. The prototype solar reactor

3.1. Solar reactor concepts

As mentioned in the introduction, there are several concepts of solar reactors that have been developed and investigated by various research groups. When designing a solar reactor for solar fuels production via thermochemical redox reactions some of the points that should be considered are: (i) accommodation of as much active material as possible in a given volume combined with maximum accessibility from the gas flow, (ii) material durability, (iii) minimization of pressure drop (e.g. structured reactors vs powder reactors), (iv) heat recovery potential, (v) possibility for continuous operation, (vi) reactor reliability and practicality, (vii) operational and technical simplicity for technology demonstration and scale-up.

3.2. Reactor design

Based on the aforementioned considerations, the reactor concept developed and employed for the redox thermochemical H_2O and CO_2 splitting reactions in the solar simulator facility is a tubular configuration with a cavity. The core component of the reactor is the redox material (in the current work $NiFe_2O_4$), which is shaped into different monolithic structures and indirectly heated.

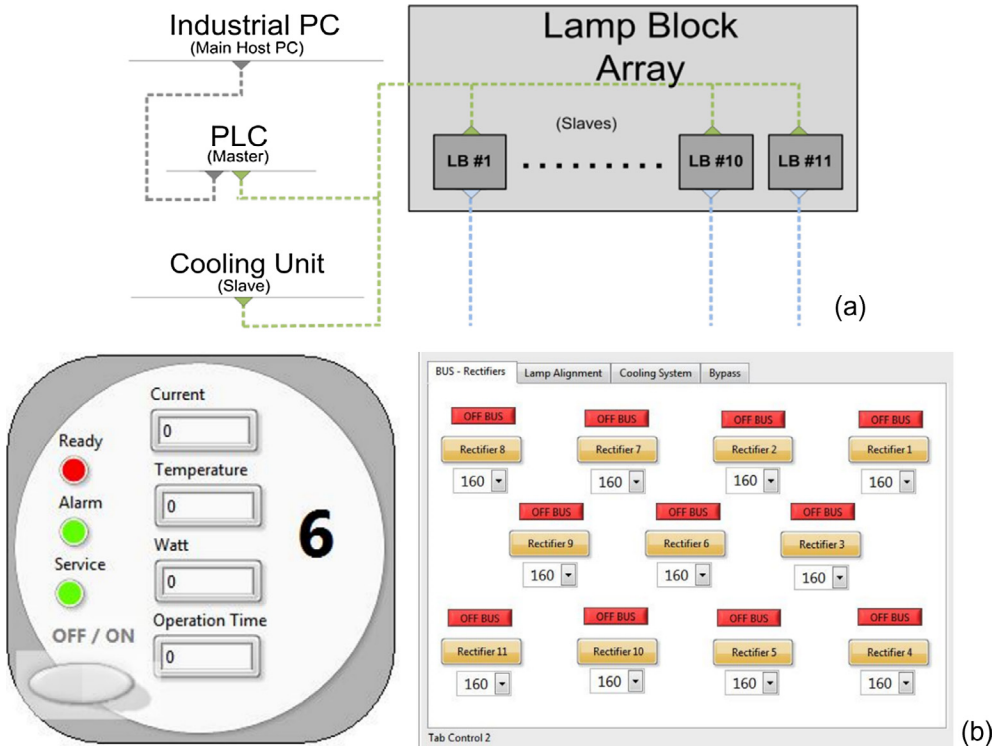

Fig. 8. Solar simulator (a) network logic and (b) detail of overall control panel.

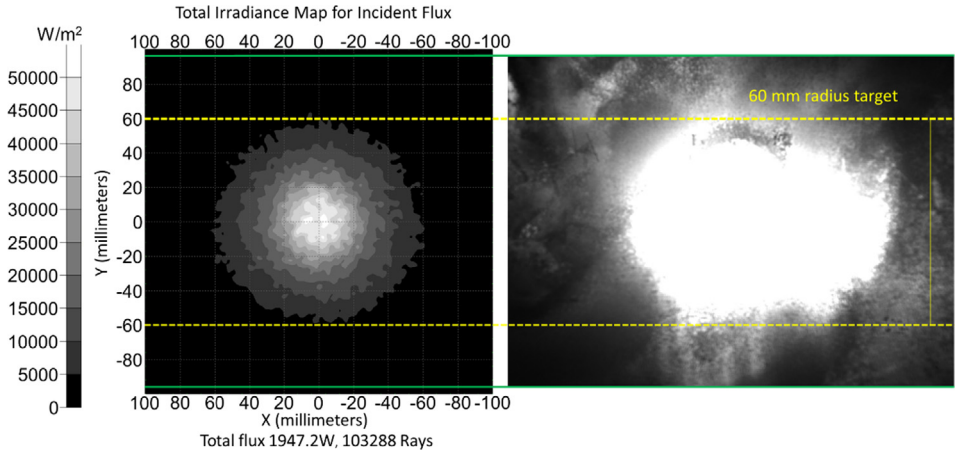

Fig. 9. Validation of reflector design, image of the 60 mm radius target in experiment.

The monoliths are placed inside an inert ceramic tube capable of withstanding and absorbing the concentrated solar irradiation at the focus. For the inert tube, non-porous Al_2O_3 (99.8% Alumina Furnace Tube, <0.5%vol porosity), was chosen over other better heat conducting materials (e.g. silicon carbide) to avoid unwanted side reactions (oxidation of the tube material) during the high temperature reduction step. Other main components of the reactor are the cavity and two inert ceramic monoliths (Al_2O_3) that are placed upstream and downstream of the active redox monolithic structure, acting as heat exchangers. The heat exchange is facilitated through switching the gas feed inlet during the splitting and reduction steps. The operation principle and a schematic of the reactor are shown in Fig. 10.

The main advantages of the specific reactor concept are the following:

- The simple and practical tubular design allows the easy interchange of reactor modules (tubes) for testing different materials (shaping methods or formulations).
- The redox material is shaped into monolithic structures, which is expected to enhance long term thermal stability and cyclability of continuous water and carbon dioxide splitting steps.
- All materials used in the reactor construction are "standard" high temperature materials manufactured at a (semi-) industrial scale, readily available. No exotic, difficult to manufacture, extremely expensive, or otherwise restricted materials or structures are used.
- In its simple lab scale version the reactor has no moving parts.
- The scale-up of the reactor can be accomplished by adjusting the cavity to the focal area of the plant (solar tower) and by adding more tubes and/or increasing their diameter.

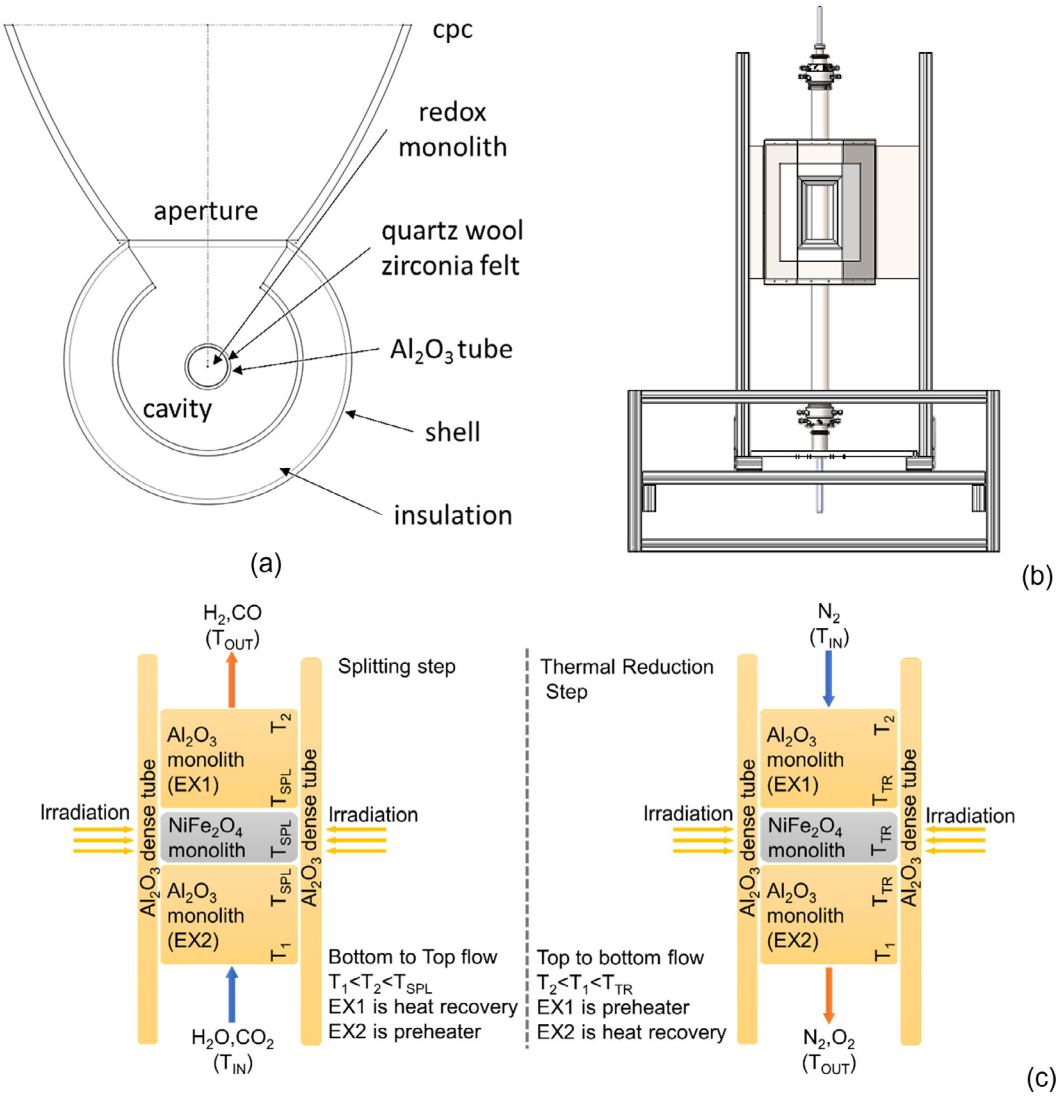

Fig. 10. (a) Schematic of the reactor concept with main components, (b) 3D model of the reactor without aperture and (c) schematic of the redox material inside the Al_2O_3 tube, with Al_2O_3 monoliths upstream and downstream.

- The use of a quartz window, although it increases thermal efficiency, since it limits convection losses, is not critical to the present reactor setup operation.

On the other hand the disadvantages of the current reactor design are:

- The ratio of the structured material to the total reactor volume is lower, compared to that of volumetric receivers (where the structured material and the reactor volume are equal). Therefore, due to the indirectly heating concept energy is consumed not only for the increase of the temperature of the active material (as in the case of the direct heating reactor concepts such as the volumetric receivers) but also for the heating of the practically inert mass of the reactor assembly (the tube, the cavity, the insulating material, etc.). This may result to a lower yield of produced fuel per reactor redox mass.
- Lower thermal efficiency compared to volumetric receivers.
- Slower reactor heat-up due to large inert mass that has to be brought to set point temperature.
- Heat-up/cool-down rates are limited by alumina tube specifications (e.g. 15 °C/min for safe long-term operation, although in practice ramps of 50 °C for short times have been used without any problem so far).
- Not enough data on long term life of alumina tube after exposure on continuous heating cooling cycles under concentrated irradiation.

Overall, a compromise has been made between theoretical targets and practical issues, leading to a reactor design that is technically simple, can be operated easily, can be cycled continuously for long periods of time and carries the promise of scale-up.

3.3. CPC & aperture

The ray tracing calculations along with measurements of the spot size (60 mm radius) allow the determination of an appropriate aperture. The solar simulator, when all lamp blocks are focused at a single spot, creates an acceptance angle at the focal plane of approximately 35°. Using these data as input, a Compound Parabolic Concentrator (CPC) is designed and evaluated as shown below (Fig. 11).

The evaluation results of the proposed CPC for a single target are shown in Fig. 12 and Table 5:

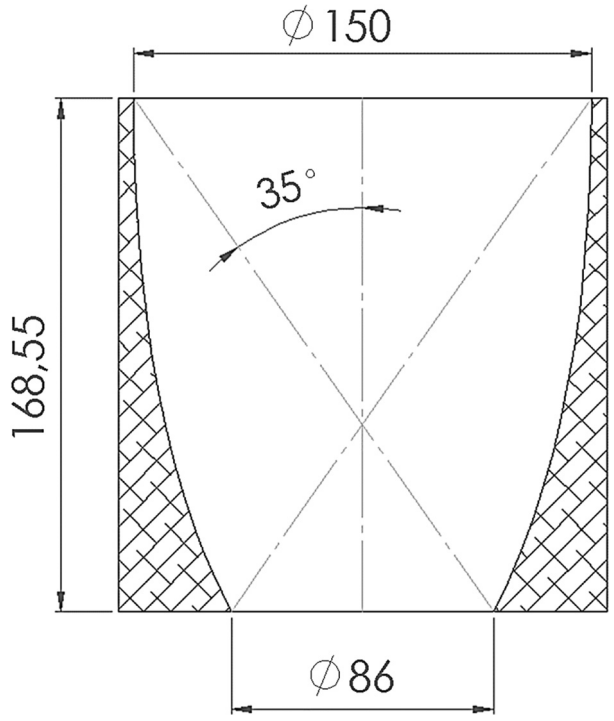

Fig. 11. design sketch of the CPC.

The CPC although designed was not constructed and used for the needs of the present study, since enough power with a rather homogenous distribution was reaching the reactor unit. Since no CPC is installed, the reactor aperture is set at 80 mm diameter, slightly larger than the inner spot size.

3.4. Thermal modelling

The concept of heat transfer to the reactor unit is that concentrated radiation from the solar simulator enters the cavity through the aperture and irradiates the front part of the alumina tube where the redox monolith is located. The rear side of the alumina tube is also irradiated by reflected radiation and re-radiation of the cavity walls. The cavity consists of an octahedron of white insulating material and the reactor tube is placed within the center of the cavity. One side of the octahedron bears the aperture where concentrated radiation enters and re-radiation from the tube and walls exits.

Only the thermal needs of the high temperature step are calculated, since this is the energy intensive step and the splitting step can in principle be performed while the system is in cooldown. The calculation of the thermal needs of the reactor is broken into four terms, (i) the thermal energy needed to keep the alumina tube at 1400 °C under continuous gas flow, with convection losses to the environment at ambient temperature, (ii) radiation losses from the tube at 1400 °C to the environment through the cavity's aperture, (iii) the energy required to perform the reduction of the monolith (enthalpy of reduction) and (iv) the energy absorbed by the cavity walls and lost to the environment through convection and re-radiation through the aperture.

The basis for the calculation of the first term is the rate of heat transfer in a typical hollow cylinder with convection and conduction both inside and outside of the cylinder. This structure is identical to the prototype assembly. The heat transfer equation is applied to each domain of the alumina tube (monolith section, upstream section and downstream section). For each domain, the flow regime of N_2 is calculated and from this the appropriate Nusselt number correlation is adopted. Setting up the geometry and running a simulation of thermal reduction at 1400 °C under steady state conditions, the temperature profiles and energy demands of each domain are calculated (Fig. 13).

The thermal needs of a free standing -not installed in the cavity-reactor unit, to maintain the high temperature (1400 °C) of the reduction step in the monolith, while exposed to N_2 gas flow is calculated at 7.7 kW_{th}, not including any radiation losses.

The second term is calculated for the reactor tube installed in a perfect cavity (circular reflecting cavity walls) from the Stefan-Boltzmann law for the cavity aperture and is calculated at 2.1 kW.

The third term is calculated from the reduction enthalpy of $NiFe_2O_4$ ($\Delta H_{redNiFe2O4}$ = 416 kJ/0.5 mol O_2 (Dimitrakis et al., 2016) and a simulation run of the $NiFe_2O_4$ monolith kinetics (Kostoglou et al., 2014) and is negligible compared to the other terms.

The fourth term was estimated to 20% of the total energy needs considering the absorptivity/emissivity and thermal conductivity of the white insulating material that forms the cavity walls.

Adding all the above terms, the thermal power needs of the prototype reactor for the energy intensive step were calculated at 12 kW. Additionally, raytracing calculations of the alumina tube and cavity are performed to ensure a relatively homogenous distribution of the incoming radiation onto the front and back side of the tube when the cavity reactor aperture is placed in the focal plane of the high power solar simulator (see Fig. 14).

3.5. Reactor control

Three thermocouples are installed within the reactor cavity and two thermocouples are used to monitor and control the reactor core temperature (upstream and downstream), one located directly below the monolith and one right above, in contact with the redox material.

The lamp blocks of the solar simulator unit are switched on/off and focused/defocused to achieve the desired temperature ramp or constant temperature in the monolith as measured by the two thermocouples. Additionally, a software with a graphic user interface was developed to allow the control of the water and nitrogen valves, heated lines, monitor temperatures and pressure and store reactor data (see Fig. 15).

4. Experimental

4.1. $NiFe_2O_4$ redox structures

Three different structures (foam, extruded honeycomb monolith, cast monolith), consisting entirely of $NiFe_2O_4$, were evaluated in the tubular reactor installed in the high flux solar simulator. The techniques used for the manufacturing of the various structures were: (i) the conventional manufacturing technique of the "replication of polymer foams" as molds for the preparation of open-cell $NiFe_2O_4$ foam with pore density of 10 ppi (pores per linear inch) (Schwartzwalder and Somers, 1963); (ii) the extrusion process for the manufacturing of a 90 cpsi (cells per square inch) $NiFe_2O_4$ honeycomb monolith (Karagiannakis et al., 2016; Pagkoura et al., 2015), similarly to what is commonly used for the manufacturing of numerous technical ceramics (e.g. Cordierite, SiC, Al_2O_3, etc) for a variety of applications (e.g. automotive emission control); (iii) a casting process for the structuring of $NiFe_2O_4$ into honeycomb monolithic bodies employing specially fabricated molds via 3D-printing. In all cases the "common denominator" is that the calcined samples consist entirely of the same material formulation ($NiFe_2O_4$).

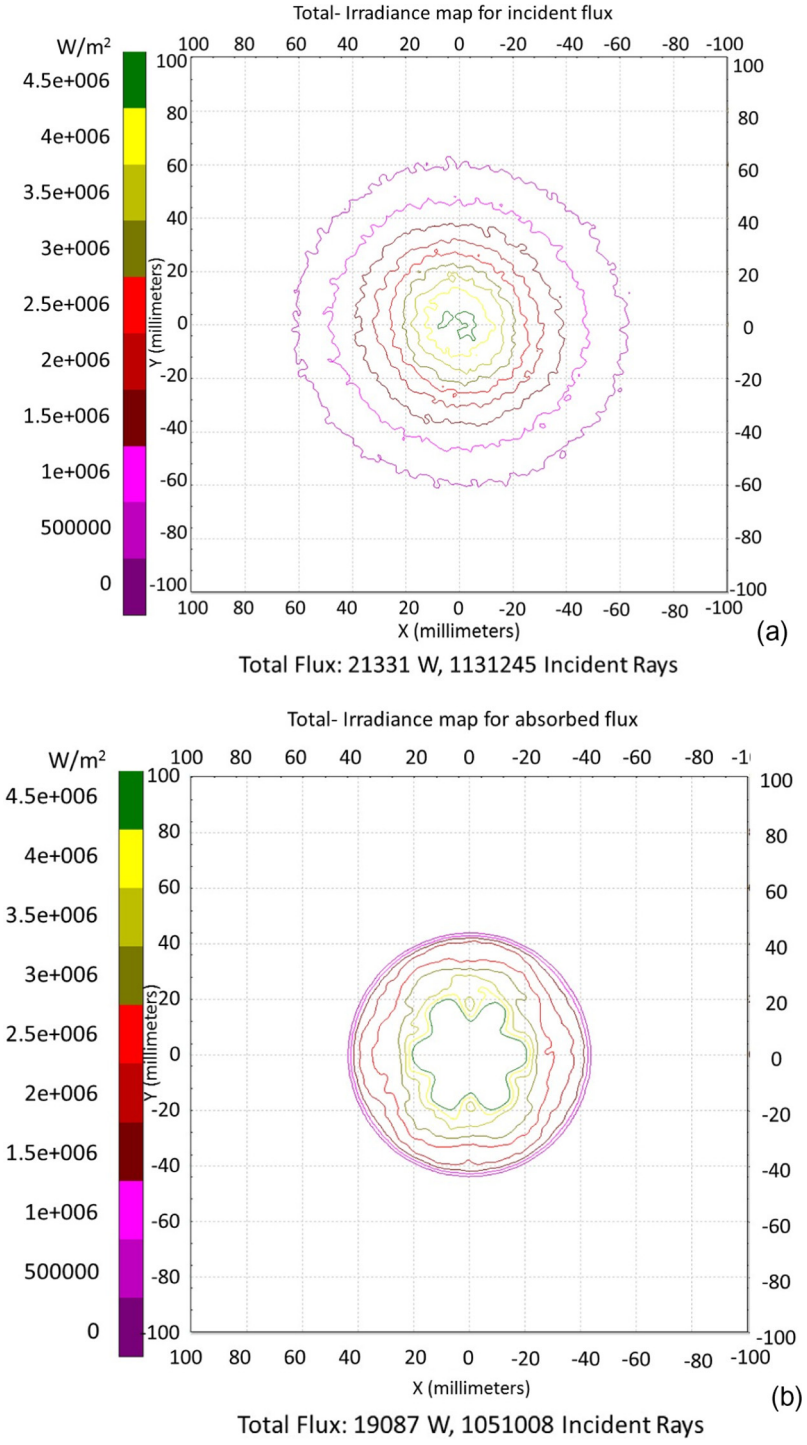

Fig. 12. Total irradiance map (a) without and (b) with CPC.

Table 5
Comparison of spot with and without CPC at 3000 mm focal distance, 200 × 200 mm target, xenon lamp 50% efficiency (3000 W) × 11 lamps.

	No secondary concentrator	Proposed CPC at focal plane
Total power absorbed	21,331 W	19,087 W
Outer spot radius	60 mm @0.5 MW/m^2	40 mm @0.5 MW/m^2
Inner spot radius	30 mm@2 MW/m^2	30 mm@2 MW/m^2
Hot spot radius	10 mm @4.5 MW/m^2	20 mm @ > 4.5 MW/m^2

A schematic of the various structures is shown in Fig. 16. Some basic characteristics of the samples are presented in Table 6.

All samples, prior to their redox activity assessment, were calcined at 1400 °C for 2 h under air to attain their fully oxidized form and to deliberately pre-expose them to the upper threshold of the thermal reduction step. This is standard practice to verify stability of the formulations and to minimize properties' change and subsequent performance variations induced by the high temperatures of the consecutive thermochemical cycles (e.g.

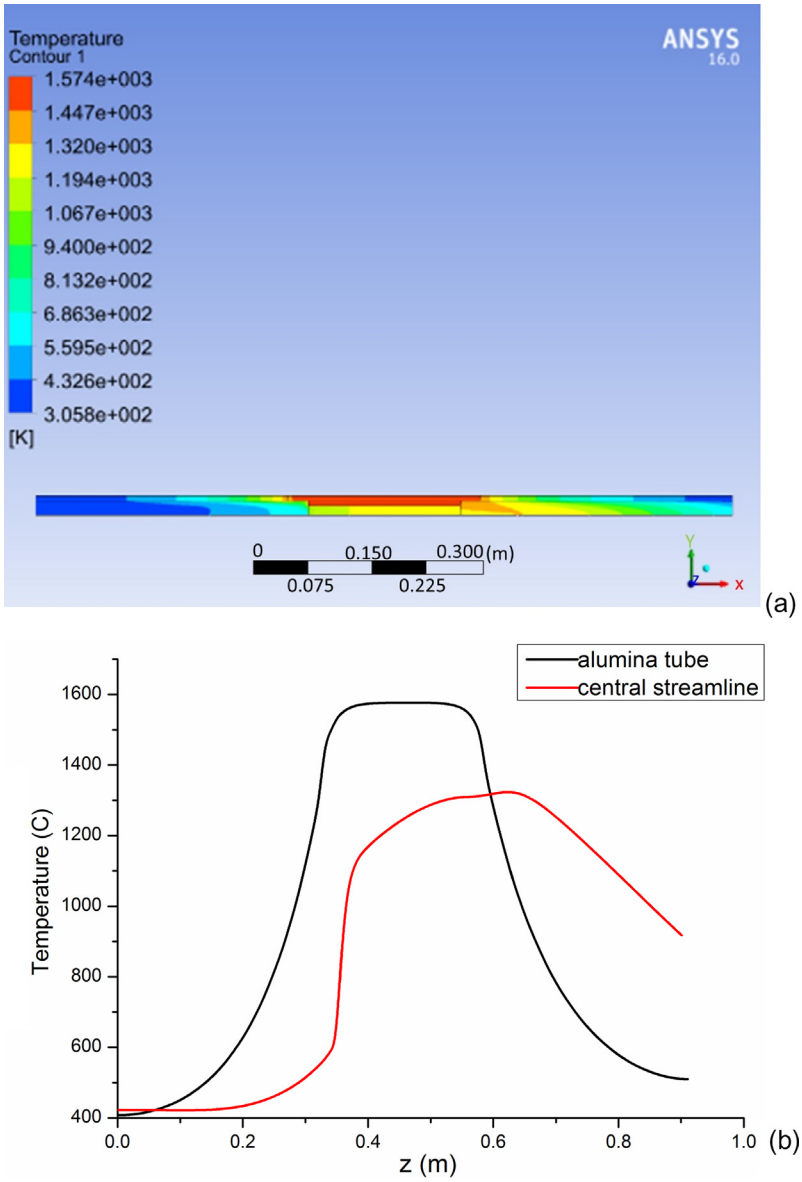

Fig. 13. Temperature distribution of the reactor (a) contour plot of slice of revolution and (b) along z axis.

sintering, surface area loss, phase segregation, etc.) (Agrafiotis et al., 2012). All samples were evaluated under the same protocol, as described below.

4.2. Redox activity assessment

Fig. 17 shows the integrated set-up of the reactor testing rig and the high-flux solar simulator. Three thermocouples (top, center, bottom) are installed in the cavity measuring the cavity's temperature. The center cavity thermocouple had the highest value compared to the top and bottom cavity thermocouples during the experiments (Fig. 18). In addition, inside the reactor, thermocouples upstream and downstream of the redox material are used to monitor the reactor's temperature. Temperature control of the reactor was conducted with the downstream thermocouple. The targeted temperatures for the isothermal steps were achieved via focusing the lamps of the simulator towards the higher temperature step (reduction) and defocusing/switching off towards the lower temperature step (splitting).

The initial step was thermal activation, during which N_2 flow passed through the sample. Temperature was increased from ambient to 1400 °C with an average heating rate of 25 °C/min (in some occasions, heating rates of 45–50 °C/min were also applied). Then the temperature was reduced to 1100 °C where the splitting step took place (Fig. 18). It can be observed that the temperature inside the alumina tube, during the thermal reduction step, was close to the temperature measured outside the tube with the center cavity thermocouple. On the other hand, during the splitting step, the temperature measured with the center cavity thermocouple is higher than that of the reactor. The focus of the simulator lamps is located at the center of the reactor aperture and the cavity sustains the reactor at the high temperature. During the splitting step, the cavity is hotter than the alumina tube, hence the higher temperature of the center cavity thermocouple in Fig. 18.

Comparison of the temperature profile recorded during the solar-simulator experiments inside the reactor with a similar protocol (i.e. $T_{splitting}$ = 1100 °C and $T_{reduction}$ = 1400 °C) conducted in the conventional electrical furnace (Fig. 19) showed that a

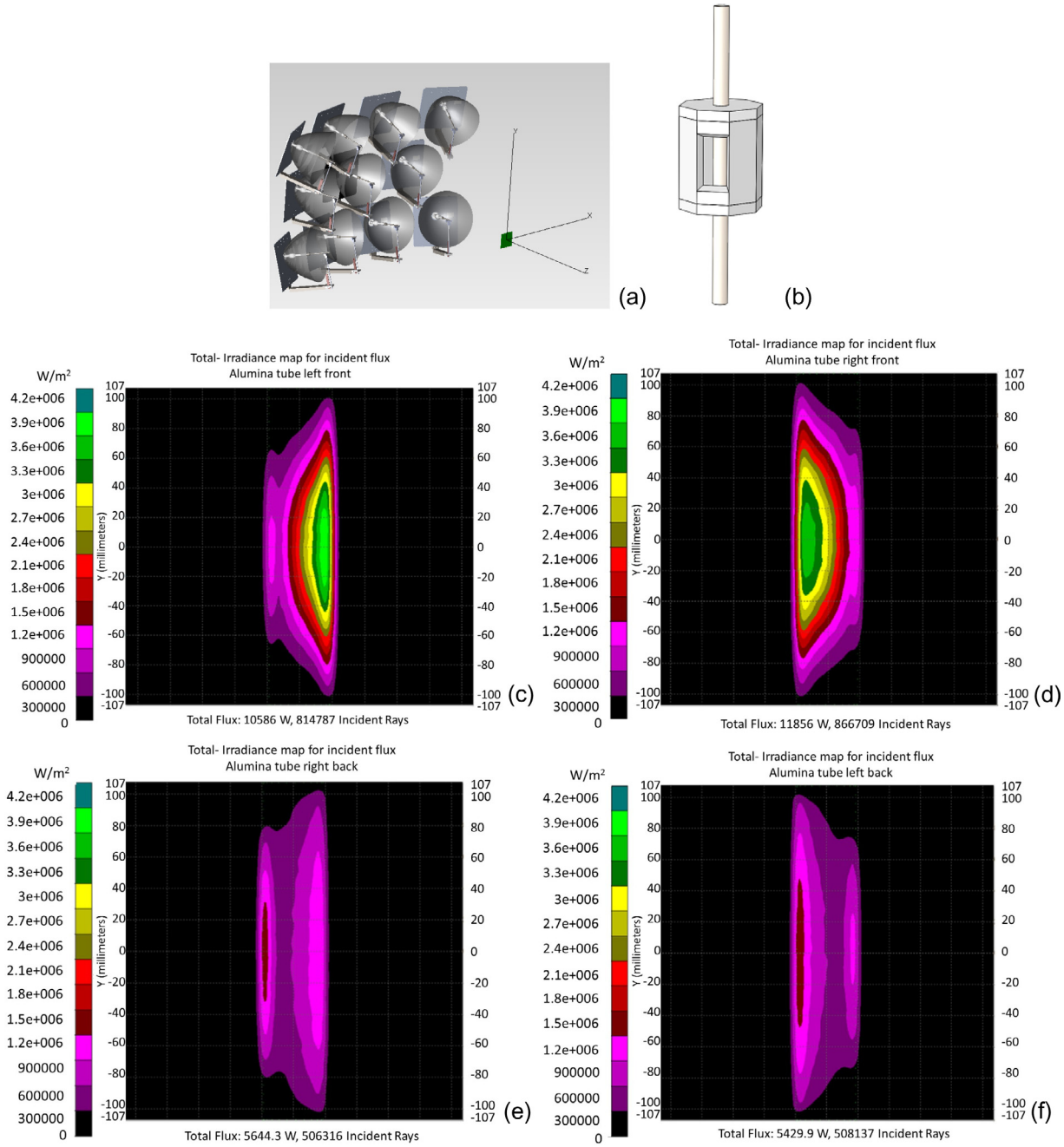

Fig. 14. (a) 3D model of the solar simulator used for ray tracing, (b) 3D model of reactor cavity and alumina tube, and flux distribution on the alumina tube (c) front left, (d) front right, (f) back left and (e) back right face.

sufficient control of the temperature inside the reactor could be achieved by regulating the flux that is directed to the cavity via continuous adjustment of the number of operating lamps and their focusing position.

Moreover, the solar simulator offers an additional degree of freedom by allowing experiments with high heating rates that cannot be achieved with the use of standard electrical furnaces (Fig. 19). However, since the reactor concept employed in the current work is a ceramic tubular reactor, extremely high heating/-cooling rates were avoided in order to secure the integrity of the material, although short-term rates of ±60 °C/min were also applied.

Based on the experimental data, and taking into account the number of lamps employed to reach the reduction step temperature, the power required is calculated at 13.5 kW (see Fig. 20), which is in accordance to the respective value calculated for the reactor in Section 3.4.

The duration of the splitting step was 30 min and the oxidant concentration was for the case of H_2O 60% in N_2 at a total flow rate of 2.94 L min^{-1}. In the case of CO_2 splitting, a 100%CO_2 bottle was used with a CO_2 flow rate of 2 L min^{-1}, while in the co-feeding experiments H_2O and CO_2 were introduced at a 2:1 volumetric ratio and a concentration of 32%H_2O and 16%CO_2 in N_2 (total flow rate 2.94 L min^{-1}). An in-house built controllable heated pressurized water tank was employed to achieve the targeted steam concentrations. The oxidation reaction was followed by a 30 min thermal reduction step at 1400 °C. Approximately ten redox cycles were implemented for each sample. The reaction products, after

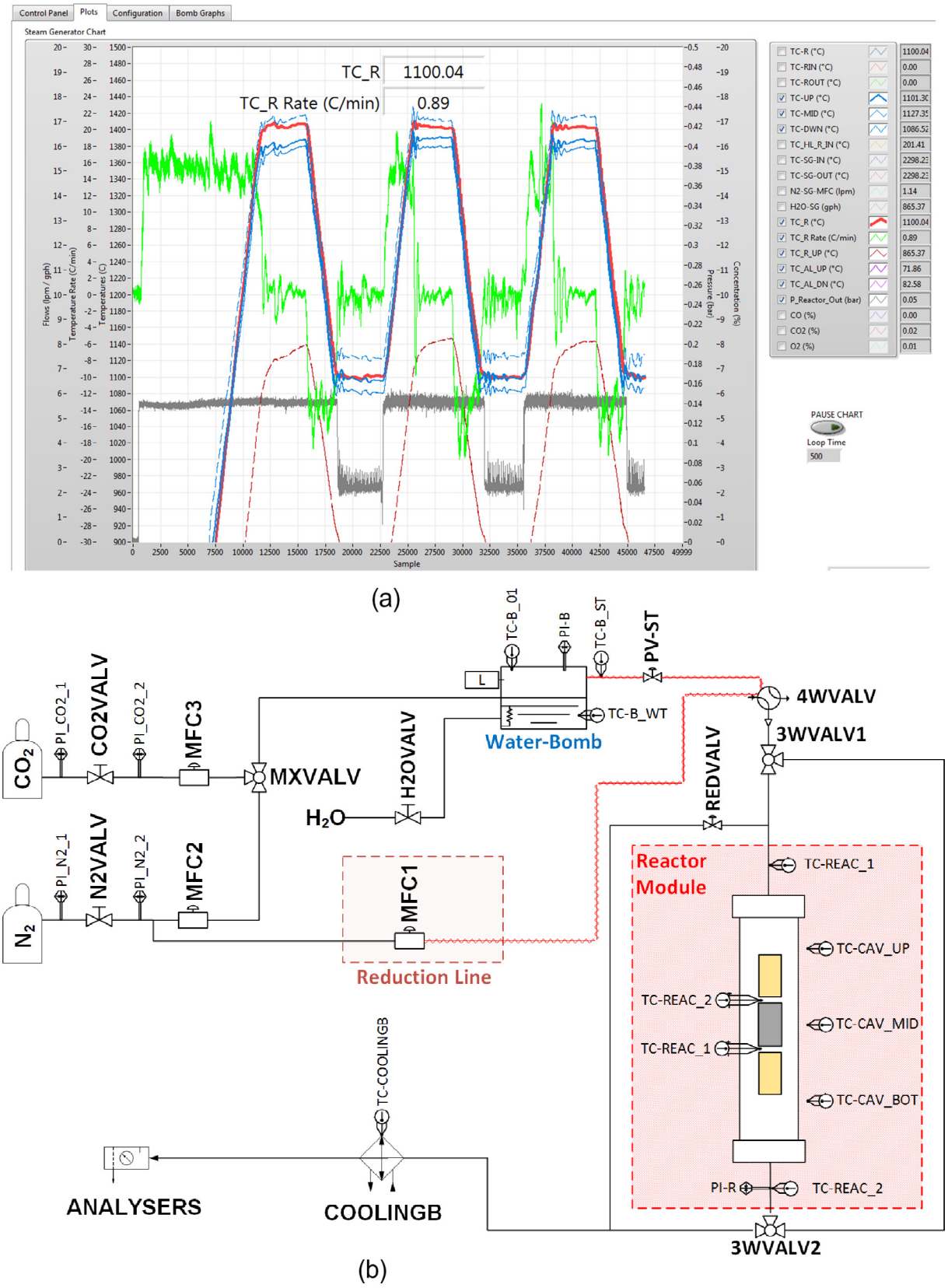

Fig. 15. (a) temperature profiles of the monolith within the alumina tube during cyclic operation, (c) the interface of the reactor control software, (d) simplified Piping and Instrumentation diagram of the solar reactor setup.

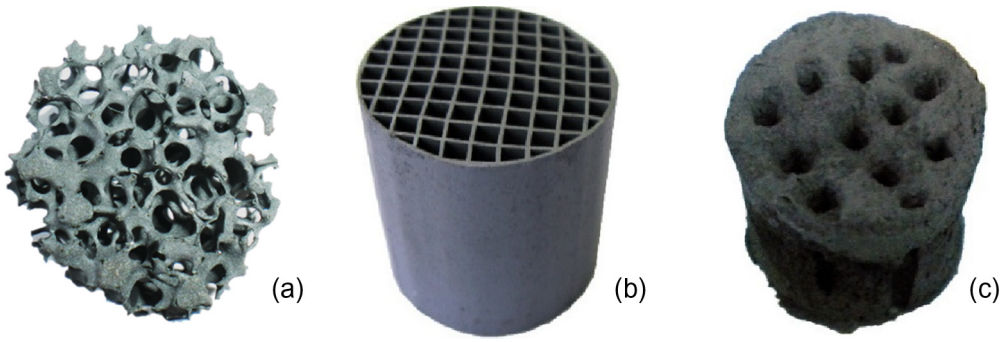

Fig. 16. Different $NiFe_2O_4$ structured bodies: (a) foam, (b) extruded honeycomb monolith, (c) 3D3 cast monolith.

Table 6
Specific characteristics of $NiFe_2O_4$ structured bodies.

	Particle mean diameter (μm)	Pores per inch (ppi)	Cells per square inch (cpsi)	Wall thickness (mm)	Porosity (%)	Weight-to-Volume ratio (g/cm^3)
Foam	5	10	–	–	–	0.77
Extruded honeycomb monolith	5	–	90	0.47	31	1.47
3D3 Cast monolith	30	–	–	–	–	2.34

Fig. 17. High-flux solar simulator and reactor integrated set-up.

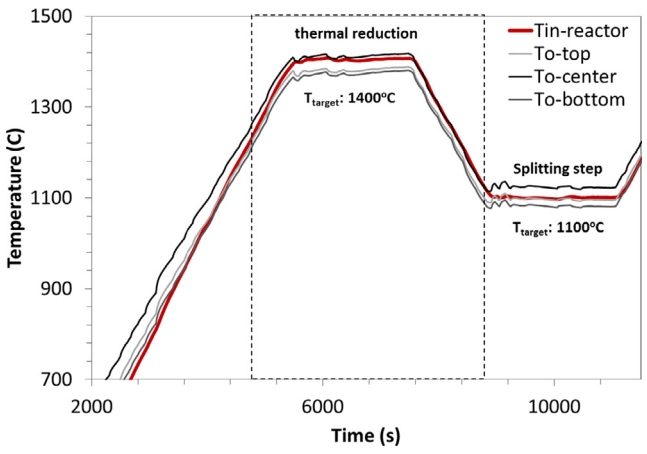

Fig. 18. Temperature profile measured with the thermocouple downstream of the sample and the cavity thermocouples during heating, cooling and isothermal steps for splitting and thermal reduction.

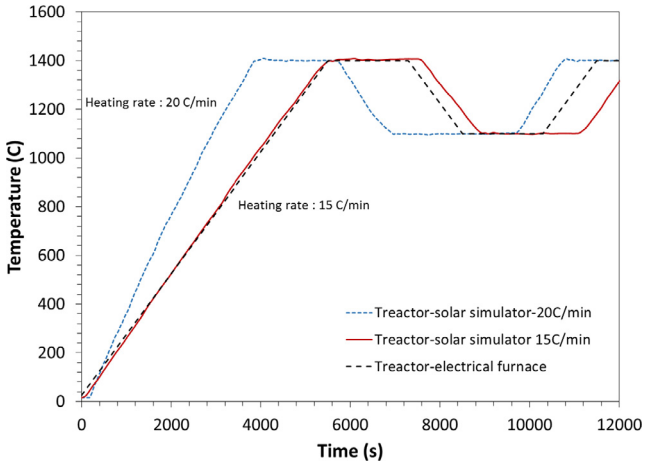

Fig. 19. Comparison of temperature profile measured with the thermocouple downstream of the sample for the case of the solar simulator and electrical furnace experiments.

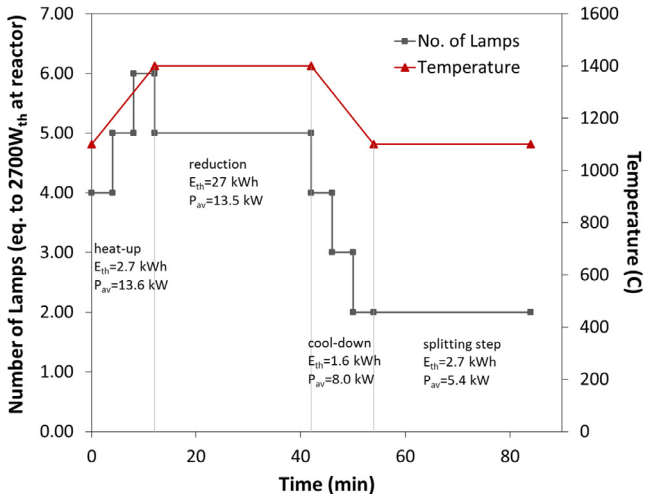

Fig. 20. Power and corresponding temperature profile during a typical cycle.

passing through a water trap, were measured with a mass spectrometer (Pfeiffer Omnistar Quadruple Mass Spectrometer) and a CO analyzer (SIGNAL 7000FM).

5. Results and discussion

5.1. H_2O splitting

Fig. 21 shows the typical H_2 and O_2 evolution profiles for the case of the foam, the extruded honeycomb monolith and the cast monolith (3D3), during the splitting with a 60% H_2O concentration in N_2 and the reduction step respectively.

The H_2 and O_2 production curves have different slopes which is observed in all structured bodies and is the result of the difference in the kinetics of the two reaction steps (the H_2O splitting reaction is faster than the thermal reduction reaction, as also reported in other works e.g. (Kostoglou et al., 2014; Neises et al., 2009; Go et al., 2008).

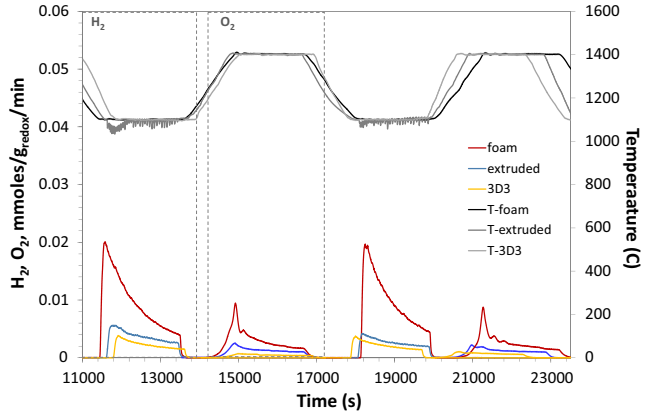

Fig. 21. Typical H_2 and O_2 and temperature profiles during H_2O-splitting (60% H_2O in N_2) and thermal reduction for the three different structures.

The H_2 concentration, during the H_2O splitting step, reaches a peak and then decreases exponentially. The decrease in the H_2 production is caused by the exhaustion of O-vacancies that are available at the specific water pressure and temperature and can receive O-atoms during the splitting step. Similarly in the case of thermal reduction, since it is endothermic, the O_2 concentration increases as temperature increases from the splitting step (1100 °C) towards the reduction step (1400 °C), reaches a peak and starts to decrease at the isothermal step. The extent of reduction of the structures depends on the temperature and the duration of the isothermal step.

The integral of the H_2 and O_2 curves describes the amount of H_2 and O_2 produced during the oxidation and reduction steps. The production of H_2 and O_2 is expressed in different forms in the literature (e.g. ml H_2 or O_2/g_{redox}, μmole H_2 or O_2/g_{redox}). In the current work, the amount of the products of the reactions is presented in mmoles/g_{redox}, where g_{redox} is the total weight of the structured bodies.

The H_2 evolution profiles vary significantly between the different structures. The most profound difference related to the production of H_2 from the $NiFe_2O_4$ foam (Fig. 21). The very open structure of the foam allows a higher degree of contact of the redox material with H_2O leading to a higher H_2 yield. In the case of the other three monolithic structures, it can be observed that the H_2 evolution curve has a smoother slope and the yield is much lower compared to that of the foam.

The amount of O_2 evolved during the thermal reduction step originates from the oxygen that has been removed from the H_2O molecules during the splitting step (i.e. it is relative to the H_2 yield). An additional contribution to the evolution of O_2 during the thermal reduction step originates from the oxygen contained in the bulk of the material (internal region Kostoglou et al., 2014) that has not been exhausted during the initial activation step where all materials are thermally reduced for 1 h (as described in the experimental section). The H_2:O_2 ratio for the case of the different structures was close to what would be expected from the theoretical stoichiometry (i.e. H_2:O_2 = 2.00). The 3D3 cast monolith had a H_2:O_2 ratio 2.00, the extruded monolith had 1.65 and the foam had 2.46. The different values of H_2:O_2 ratio for the different samples could be attributed to variations in the oxygen contained in the bulk of the different structures, variations in the structural characteristics of the monoliths (e.g. different scales of porosity of the redox struts for the case of the foam, or the redox walls for the case of the extruded and the 3D-cast monoliths) or variations in the homogeneity of the temperature that is reached in the bulk and on the surface of the structured body during the thermal reduction steps which in turn may lead to insufficient reduction. It is expected that the exhaustion of the oxygen contained in the bulk of the monolithic structures after multiple cycles will lead to the stabilization of the H_2:O_2 ratio around the stoichiometric value 2.00.

The activity of the redox structures, if the H_2 yield is expressed in terms of redox material weight (i.e. mmoles/g_{redox}), follows the order: foam ≫ extruded monolith > 3D3.

Table 7
Total H_2 yield expressed in terms of structure weight and volume.

		Total H_2 yield/cycle			
Conditions	$NiFe_2O_4$ structures	mmoles/g_{redox}	Difference from $NiFe_2O_4$ foam	mmoles/ml_{redox}	Difference from $NiFe_2O_4$ foam
$T_{splitting}$ = 1100 °C	Extruded monolith	0.083	−71%	0.122	−44%
60% H_2O	Foam	0.289	0	0.217	0
	3D3	0.070	−76%	0.164	−24%

As shown in Table 6, the bulk density of the structures (weight-to-volume ratio) is different for each structure. The $NiFe_2O_4$ foam has the lowest bulk density while the cast monoliths have the highest. Consequently, if the H_2 yield is expressed as a function of the volume of the redox material (i.e. mmole/ml_{redox}) instead of the weight, the relative activity of the structures changes. The foam is still the most active structure, but the gap with the other structures is significantly reduced (Table 7).

Thus, it can be argued that expressing the evolution of H_2 as a function of the volume of the structure and not the mass in the case of structures consisting entirely of the redox material may be more representative when describing a solar structured reactor.

An evaluation of the relative performance of the materials reported here with results reported in the literature is not straightforward, since experimental conditions vary from one study to the other (i.e. space velocities, reactant concentrations, temperatures, test rigs, direct vs indirect heating concepts, etc.). However, compared to other relatively relevant works reported in literature e.g. (Gokon et al., 2009; Gokon et al., 2011; Kawakami et al., 2014) that deal with $NiFe_2O_4$ foams, the activity of the best structure reported in the current work leads to a maximum H_2 production rate of 20 μmoles/min/g_{device} or 0.45 ml/min/g_{device} (where, device: $NiFe_2O_4$ foams) respectively, i.e. approximately 4 times higher than the results reported in the literature so far (shortly mentioned in the introduction section). The total H_2 yield of the $NiFe_2O_4$ foam (i.e. 7.35 ml/g_{device}) was approximately 1.5–7 times higher compared to the values reported in Gokon et al. (2011). In addition, comparison of the $NiFe_2O_4$ foam with foams constructed from other materials, such as CeO_2 (Chueh et al., 2010), shows that there is significant difference of the production rate for the latter (CeO_2 foam has faster H_2 production rate), however with a lower total H_2 yield (4.6 ml/g_{device} for the CeO_2 foam and 7.35 ml/g_{device} for the $NiFe_2O_4$ foam).

5.2. CO_2 splitting

Similarly to the H_2 evolution curves, CO evolved during the splitting of CO_2 (100% CO_2) on the different structured bodies (Fig. 22). On the contrary, however, to the H_2 profiles, CO curves were sharper. This behavior is more profound in the case of the foam. The fact that the CO evolution profile is steeper than that of H_2 originates from the high concentration of CO_2 (100%CO_2 compared to 60%H_2O), as it has been observed in previous CO_2 splitting experiments with different CO_2 concentrations over $NiFe_2O_4$ powder (Lorentzou et al., 2013).

The trend in the structures' activity for the splitting of 100% CO_2 (Table 8), is maintained as in the case of the H_2O splitting with 60% H_2O (Table 7). However, the total yield of CO is lower compared to the respective H_2 yield during H_2O splitting (despite higher CO_2 concentration), which can be attributed to the more favorable thermodynamics of WS (Lange et al., 2016).

In contrast to the comparison with other works in the literature that was presented for the case of H_2O splitting, there are no relative articles that deal with the splitting of CO_2 using $NiFe_2O_4$ structured monolithic bodies. However, CO_2 splitting on structured reactors has been investigated on CeO_2 foams (as described in the introduction). Compared to (Furler et al., 2012), the CO total yield reported for the $NiFe_2O_4$ foam was approximately 2.5 times higher (i.e. 3.7 ml/g_{device} for the $NiFe_2O_4$ foam presented in this work compared to 1.465 ml/g_{device} for CeO_2 foam reported in Furler et al. (2012)) for material that was previously regenerated at around 1400 °C.

5.3. H_2O-CO_2 co-feeding

In the case of the simultaneous H_2O and CO_2 splitting (co-feeding) experiments, the reactants mixture used was 16%CO_2-32%H_2O. In all cases, the H_2 and CO profiles were parallel to each other, with CO yield being somewhat lower compared to the H_2 yield, as expected (see Figs. 23–25).

The H_2/CO yield ratio calculated for all structures is presented in Table 9 along with the H_2 and CO total yield. It is noted that for a H_2O/CO_2 ratio of 2.0 (feed composition in the current work), the H_2/CO yield ranges from 1.13 for the case of the extruded monolith to 1.26 for the foam and 1.17 for the 3D3 cast monolith, which is in

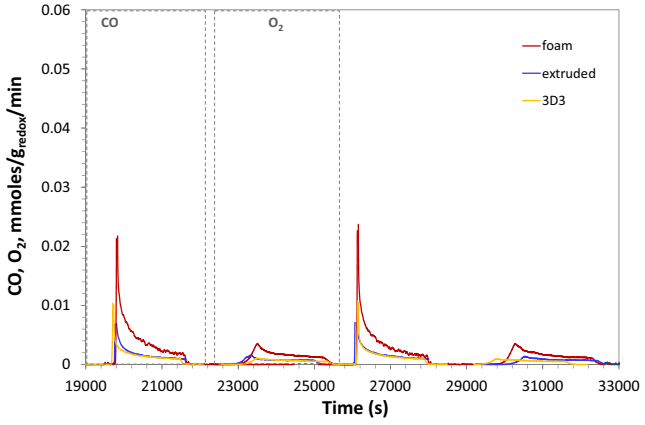

Fig. 22. Typical CO and O_2 profiles during CO_2-splitting (100%CO_2) and thermal reduction for the three different structures.

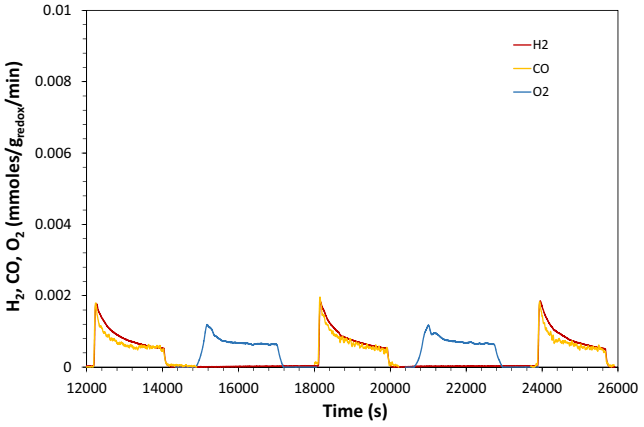

Fig. 23. Consecutive H_2 and CO evolution curves during simultaneous H_2O and CO_2 splitting on the $NiFe_2O_4$ extruded monolith structure.

Table 8
Total CO yield expressed in terms of structure weight and volume.

		Total CO yield/cycle			
Conditions	$NiFe_2O_4$ structures	mmoles/g_{redox}	deviation from $NiFe_2O_4$ foam	mmoles/ml_{redox}	deviation from $NiFe_2O_4$ foam
$T_{splitting}$ = 1100 °C	Extruded monolith	0.055	−59	0.081	−23
100% CO_2	Foam	0.137	0	0.106	0
	3D3	0.048	−65	0.112	5

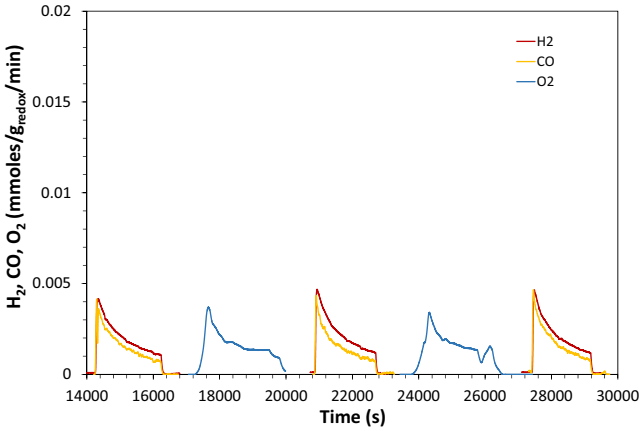

Fig. 24. Consecutive H_2 and CO evolution curves during simultaneous H_2O and CO_2 splitting on the $NiFe_2O_4$ foam structure.

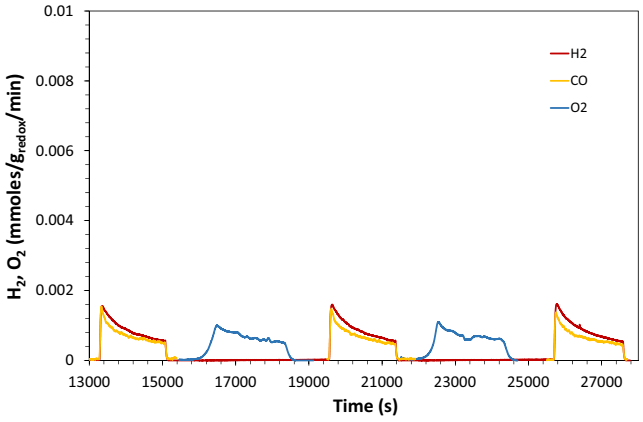

Fig. 25. Consecutive H_2 and CO evolution curves during simultaneous H_2O and CO_2 splitting on the $NiFe_2O_4$ 3D3 cast monolith.

accordance to the results presented in Lorentzou et al. (2013) for $NiFe_2O_4$ powder where the H_2/CO ratio was ~1.4. This variation in the H_2/CO ratio can be attributed to the variation in the actual temperature of the samples, caused by the solar simulator flux control and differences in the transfer of heat in the whole mass of each structure (very open structure of foam compared to the more dense honeycombs).

The simultaneous introduction of H_2O and CO_2 for the production of syngas on structured reactors has been reported previously on CeO_2 felt structures (Furler et al., 2012). The total H_2 and CO yield for the case of the $NiFe_2O_4$ foam in terms of ml of product/g_{device} was 1.55 and 1.2 respectively, which is lower compared to the CeO_2 felt examined in Furler et al. (2012) (2.21 ml H_2/g_{device} and 0.94 ml CO/g_{device}). Based on these results, it seems that in the case of the $NiFe_2O_4$ foam the splitting reaction of CO_2 is favored, in contrast to the case of CeO_2 felt, however, the difference is not considered significant (approximately 12% difference between the two works).

6. Conclusions

In this work, two step solar thermochemical redox cycles for the production of H_2, CO or solar syngas on $NiFe_2O_4$ structured reactors were investigated under solar simulated conditions. The work was developed in three parts. First, the design and construction of a high flux solar simulator facility for the bridging of conventional lab-scale experiments with actual solar field experiments was presented. At the second part, a simple and practical cavity-tube solar reactor that could host the different redox structures was designed and constructed. At the third part, the solar reactor was integrated in the solar simulator test facility for two-step redox thermochemical cycles for the splitting of H_2O, CO_2 and combined feedstock.

A control strategy for the solar simulator was developed to achieve the temperature profiles required for the consecutive splitting and regeneration cycles on the structured reactor. Three different structures were evaluated with respect to their redox activity. All structures were active splitters, however as expected those with the more “open” (porous) and lighter structure were better performing when the activity was expressed in terms of weight.

In the current work, the redox material that was employed ($NiFe_2O_4$) is an active water splitter that has been widely investigated. The best performing structure was that of the $NiFe_2O_4$ foam. Low product yields, observed for the $NiFe_2O_4$ structured monoliths compared to yields reported previously for the case of $NiFe_2O_4$ powder (e.g. Lorentzou et al., 2013; Agrafiotis et al., 2012), are not only a result of the inherent chemistry of the material but also of structural limitations that inhibit the access of the reactants to the active sites. The production rates and total yields measured were of the same order of magnitude and in most cases, measurably higher compared to relative values reported in the literature. However, it should be considered that redox thermochemical reactions are particularly sensitive to variations in the experimental conditions, rendering, therefore, the comparison between different works a difficult and not straightforward task.

Nevertheless, there is a lot of potential in the optimization of the morphological and geometric characteristics of the monolithic structures in order to reach the ideal performance of powder formulations (first redox cycles only), by increasing the accessibility of the redox structured bodies from the gaseous reactants. Future work will focus on the development of novel structures consisting of different redox material formulations (e.g. cerium-based mixed oxides, $CoFe_2O_4/Al_2O_3$ oxides, perovskites, etc.) with increased surface/volume-to-weight ratio that is expected to lead to higher H_2 and CO yields.

At the reactor level, the indirectly irradiated structured reactor has the benefit of a simple and practical concept that can be easily scaled-up. However, its design should include improved heat recovery concepts that are expected to increase the overall process efficiency.

Table 9
Total H_2 and CO yield from simultaneous H_2O-CO_2 splitting.

		Total H_2 and CO yield/cycle		
Conditions	$NiFe_2O_4$ structures	H_2 mmoles/g_{redox}	CO mmoles/g_{redox}	H_2:CO ratio
$T_{splitting}$ = 1100 °C	Extruded monolith	0.026	0.023	1.13
16% CO_2-32%H_2O	Foam	0.068	0.054	1.26
	3D3	0.027	0.023	1.17

Acknowledgements

This work was partially supported by the European Commission through the European Research Council (ERC) Advanced Grant-Project ARMOS (ERC-2010-AdG 268049) and the FCH-JU through the HYDROSOL-PLANT project (GA 325361).

The authors would like to gratefully acknowledge the significant contribution of Mr C. Lekkos, Mr P. Pantelidis and Mr I. Dolios in the solar reactor-solar simulator integration for the facilitation of the solar simulated experiments.

References

Abanades, S., Charvin, P., Flamant, G., Neveu, P., 2006. Screening of water-splitting thermochemical cycles potentially attractive for hydrogen production by concentrated solar energy. Energy 31, 2805–2822.

Agrafiotis, C.C., Roeb, M., Konstandopoulos, A.G., Nalbandian, L., Zaspalis, V.T., Sattler, C., Stobbe, P., Steele, A.M., 2005. Solar water splitting for hydrogen production with monolithic reactors. Sol. Energy 79 (4), 409–421. Available at: http://dx.doi.org/10.1016/j.solener.2005.02.026.

Agrafiotis, C.C., Pagkoura, C., Zygogianni, A., Karagiannakis, G., Kostoglou, M., Konstandopoulos, A.G., 2012. Hydrogen production via solar-aided water splitting thermochemical cycles: combustion synthesis and preliminary evaluation of spinel redox-pair materials. Int. J. Hydrogen Energy 37 (11), 8964–8980. Available at: http://dx.doi.org/10.1016/j.ijhydene.2012.02.196.

Agrafiotis, C.C., Roeb, M., Sattler, C., 2015. A review on solar thermal syngas production via redox pair-based water/carbon dioxide splitting thermochemical cycles. Renew. Sustain. Energy Rev. 42, 254–285.

Alonso, E., Romero, M., 2015. Review of experimental investigation on directly irradiated particles solar reactors. Renew. Sustain. Energy Rev. 41, 53–67.

Alxneit, I., Dibowski, G., 2011. Solar simulator evaluation report. Deliverable 12.5 for Project SFERA (Solar Facilities for the European Research Area).

Carty R.H., Mazumder M.M., Schreider J.D., Panborn J.B., 1981. Thermochemical Hydrogen Production, GRI-80/0023, Gas Research Institute for the Institute of Gas Technology, Chicago, IL, 1–4.

Chueh, W.C., Falter, C., Abbott, M., Scipio, D., Furler, P., Haile, S.M., Steinfeld, A., 2010. High-Flux solar-driven thermochemical dissociation of CO_2 and H_2O using nonstoichiometric ceria. Science 330 (6012), 1797–1801. Available at: http://science.sciencemag.org/content/330/6012/1797.abstract.

Codd, D.S., Carlson, A., Rees, J., Slocum, A.H., 2010. A low cost high flux solar simulator. Sol. Energy 84 (12), 2202–2212. Available at: http://www.sciencedirect.com/science/article/pii/S0038092X10002665.

Dimitrakis, D., Lekkos, C., Dolios, I., Konstandopoulos, A.G., 2013. Design and Construction of a 66 kW Solar Simulator Facility. 9ο Πανελλήνιο Επιστημονικό Συνέδριο Χημικής Μηχανικής (9th Panhellenic Scientific Chemical Engineering Congress), May 23–25, Athens, Greece.

Dimitrakis, D.A., Tsongidis, N.I., Konstandopoulos, A.G., 2016. Reduction enthalpy and charge distribution of substituted ferrites and doped ceria for thermochemical water and carbon dioxide splitting with DFT + U. Phys. Chem. Chem. Phys. 18 (34), 23587–23595. Available at: http://dx.doi.org/10.1039/C6CP05073E.

Erickson, B., 2012. Characterization of the University of Florida Solar Simulator and an Inverse Solution for Identifying Intensity Distributions from Multiple Flux Maps in Concentrating Aolar Applications, Master's Thesis, University of Florida.

Funk, J.E., 2001. Thermochemical hydrogen production: past and present. Int. J. Hydrogen Energy 26 (3), 185–190.

Furler, P., Scheffe, J., Gorbar, M., Moes, L., Vogt, U., Steinfeld, A., 2012. Solar thermochemical CO_2 splitting utilizing a reticulated porous ceria redox system. Energy Fuels 26 (11), 7051–7059. Available at: http://dx.doi.org/10.1021/ef3013757.

Furler, P., Scheffe, J.R., Steinfeld, A., 2012. Syngas production by simultaneous splitting of H_2O and CO_2 via ceria redox reactions in a high-temperature solar reactor. Energy Environ. Sci. 5 (3), 6098–6103. Available at: http://dx.doi.org/10.1039/C1EE02620H.

Go, K.S., Son, S.R., Kim, S.D., 2008. Reaction kinetics of reduction and oxidation of metal oxides for hydrogen production. Int. J. Hydrogen Energy 33 (21), 5986–5995. Available at: http://linkinghub.elsevier.com/retrieve/pii/S0360319908005843.

Gokon, N., Takahashi, S., Yamamoto, H., Kodama, T., 2008. Thermochemical two-step water-splitting reactor with internally circulating fluidized bed for thermal reduction of ferrite particles. Int. J. Hydrogen Energy 33 (9), 2189–2199.

Gokon, N., Hasegawa, T., Takahashi, S., Kodama, T., 2008. Thermochemical two-step water-splitting for hydrogen production using Fe-YSZ particles and a ceramic foam device. Energy 33 (9), 1407–1416. Available at: http://www.sciencedirect.com/science/article/pii/S0360544208001126.

Gokon, N., Murayama, H., Nagasaki, A., Kodama, T., 2009. Thermochemical two-step water splitting cycles by monoclinic ZrO_2-supported $NiFe_2O_4$ and Fe_3O_4 powders and ceramic foam devices. Sol. Energy 83 (4), 527–537.

Gokon, N., Kodama, T., Imaizumi, N., Umeda, J., Seo, T., 2011. Ferrite/zirconia-coated foam device prepared by spin coating for solar demonstration of thermochemical water-splitting. Int. J. Hydrogen Energy 36 (3), 2014–2028.

Gokon, N., Mataga, T., Kondo, N., Kodama, T., 2011. Thermochemical two-step water splitting by internally circulating fluidized bed of $NiFe_2O_4$ particles: successive reaction of thermal-reduction and water-decomposition steps. Int. J. Hydrogen Energy 36 (8), 4757–4767. Available at: http://www.sciencedirect.com/science/article/pii/S0360319911001194.

Gokon, N., Kodama, T., Imaizumi, N., Umeda, J., Seo, T., 2011. Ferrite/zirconia-coated foam device prepared by spin coating for solar demonstration of thermochemical water-splitting. Int. J. Hydrogen Energy 36 (3), 2014–2028. Available at: http://linkinghub.elsevier.com/retrieve/pii/S0360319910022494.

Guesdon, C., Alxneit, I., Tschudi, H.R., Wuillemin, D., Petrasch, J., Brunner, Y., Winkel, L., Sturzenegger, M., 2006. PSI's 1 kW imaging furnace – a tool for high-temperature chemical reactivity studies. Sol. Energy 80 (10), 1344–1348. Available at: http://www.sciencedirect.com/science/article/pii/S0038092X05002902.

Haueter, P., Moeller, S., Palumbo, R., Steinfeld, A., 1999. The production of zinc by thermal dissociation of zinc oxide—solar chemical reactor design. Sol. Energy 67 (1–3), 161–167. Available at: http://www.sciencedirect.com/science/article/pii/S0038092X00000372.

Hirsch, D., Zedtwitz, P.v., Osinga, T., Kinamore, J., Steinfeld, A., 2003. A new 75 kW high-flux solar simulator for high-temperature thermal and thermochemical research. J. Sol.Energy Eng. 125 (1), 117–120. Available at: http://dx.doi.org/10.1115/1.1528922.

Houaijia, A., Sattler, C., Roeb, M., Lange, M., Breuer, S., Säck, J.P., 2013. Analysis and improvement of a high-efficiency solar cavity reactor design for a two-step thermochemical cycle for solar hydrogen production from water. Sol. Energy 97, 26–38. Available at: http://www.sciencedirect.com/science/article/pii/S0038092X13003071.

http://www.dlr.de/dlr/en/desktopdefault.aspx/tabid-10202/334_read-21807/#/gallery/26638/ (accessed on April 2017).

Jaworske, D.A., Jefferies, K.S., Mason, L.S., 1996. Alignment and initial operation of an advanced solar simulator. J. Spacecraft Rockets 33 (6), 867–869. Available at: http://dx.doi.org/10.2514/3.26852.

Karagiannakis, G., Pagkoura, C., Halevas, E., Baltzopoulou, P., Konstandopoulos, A.G., 2016. Cobalt/cobaltous oxide based honeycombs for thermochemical heat storage in future concentrated solar power installations: multi-cyclic assessment and semi-quantitative heat effects estimations. Sol. Energy 133, 394–407. Available at: http://linkinghub.elsevier.com/retrieve/pii/S0038092X16300652.

Kawakami, S., Myojin, T., Cho, H.-S., Hatamachi, T., Gokon, N., Kodama, T., 2014. Thermochemical two-step water splitting cycle using Ni-ferrite and CeO coated ceramic foam devices by concentrated Xe-light radiation. Energy Procedia 49, 1980–1989.

Kodama, T., Gokon, N., 2007. Thermochemical cycles for high-temperature solar hydrogen production. Chem. Rev. 107 (10), 4048–4077.

Kodama, T., Gokon, N., Yamamoto, R., 2008. Thermochemical two-step water splitting by ZrO_2-supported $Ni_xFe_{3-x}O_4$ for solar hydrogen production. Sol. Energy 82 (1), 73–79.

Koepf, E., Advani, S.G., Steinfeld, A., Prasad, A.K., 2012. A novel beam-down, gravity-fed, solar thermochemical receiver/reactor for direct solid particle decomposition: design, modeling, and experimentation. Int. J. Hydrogen Energy 37 (22), 16871–16887. Available at: http://www.sciencedirect.com/science/article/pii/S0360319912018885.

Konstandopoulos, A.G., Lorentzou, S., 2010. Novel monolithic reactors for solar thermochemical water splitting. In: Vayssieres, L. (Ed.), Invited Chapter In On Solar Hydrogen and Nanotechnology. John Wiley & Sons, pp. 623–639.

Kostoglou, M., Lorentzou, S., Konstandopoulos, A.G., 2014. Improved kinetic model for water splitting thermochemical cycles using Nickel Ferrite. Int. J. Hydrogen Energy 39 (12), 6317–6327. Available at: http://linkinghub.elsevier.com/retrieve/pii/S0360319914002018.

Krueger, K.R., Davidson, J.H., Lipiński, W., 2011. Design of a new 45 kWe high-flux solar simulator for high-temperature solar thermal and thermochemical research. J. Sol.Energy Eng. 133 (1), 11013–11018. Available at: http://dx.doi.org/10.1115/1.4003298.

Kuhn, P., Hunt, A., 1991. A new solar simulator to study high temperature solid-state reactions with highly concentrated radiation. Solar Energy Mater. 24 (1–4), 742–750. Available at: http://linkinghub.elsevier.com/retrieve/pii/016516339190107 V.

Kuhn, M., Bishop, S.R., Rupp, J.L.M., Tuller, H.L., 2013. Structural characterization and oxygen nonstoichiometry of ceria-zirconia ($Ce_{1-x}Zr_xO_{2-\delta}$) solid solutions. Acta Mater. 61 (11), 4277–4288.

Lange, M., Roeb, M., Sattler, C., Pitz-Paal, R., 2016. Entropy analysis of solar two-step thermochemical cycles for water and carbon dioxide splitting. Entropy 18 (1), 24. Available at: http://dx.doi.org/10.3390/e18010024.

Levêque, G., Bader, R., Lipiński, W., Haussener, S., 2016. Experimental and numerical characterization of a new 45 kW_{el} multisource high-flux solar simulator. Opt. Express 24, 1360–1373.

Li, J., Gonzalez-Aguilar, J., Pérez-Rábago, C., Zeaiter, H., Romero, M., 2014. Optical analysis of a hexagonal 42kWe high-flux solar simulator. Energy Procedia 57, 590–596. Available at: http://www.sciencedirect.com/science/article/pii/S187661021401580X.

Lichty, P., Liang, X., Muhich, C., Evanko, B., Bingham, C., Weimer, A.W., 2012. Atomic layer deposited thin film metal oxides for fuel production in a solar cavity reactor. Int. J. Hydrogen Energy 37 (22), 16888–16894. Available at: http://www.sciencedirect.com/science/article/pii/S0360319912017703.

Lorentzou, S., Karagiannakis, G., Pagkoura, C., Zygogianni, A., Konstandopoulos, A.G., 2013. Thermochemical CO_2 and CO_2/H_2O splitting over $NiFe_2O_4$ for solar fuels

synthesis. Energy Procedia 49, 1999–2008. Available at: http://dx.doi.org/10.1016/j.egypro.2014.03.212.
Lorentzou, S., Karagiannakis, G., Dimitrakis, D., Pagkoura, C., Zygogianni, A., Konstandopoulos, A.G., 2015. Thermochemical redox cycles over ce-based oxides. Energy Procedia 69, 1800–1809.
Loutzenhiser, P.G., Meier, A., Steinfeld, A., utzenhiser et al., 2010 b. Review of the two-step H_2O/CO_2-splitting solar thermochemical cycle based on Zn/ZnO redox reactions. Materials 3 (11), 4922–4938. Available at: http://dx.doi.org/10.3390/ma3114922.
Loutzenhiser, P.G., Meier, A., Gstoehl, D., Steinfeld, A., 2010. CO_2 splitting via the solar thermochemical cycle based on Zn/ZnO redox reactions. In Advances in CO_2 Conversion and Utilization. ACS Symposium Series. American Chemical Society, pp. 3–25.
McDaniel, A.H., Ambrosini, A., Coker, E.N., Miller, J.E., Chueh, W.C., O'Hayre, R., Tong, J., 2013. Nonstoichiometric perovskite oxides for solar thermochemical H_2 and CO production. Energy Procedia 49, 2009–2018.
Mcquillan, B.W., Brown, L.C., Besenbruch, G.E., Tolman, R., Cramer, T., Russ, B.E., Vermillion, B.A., Earl, B., Hsieh, H., Chen, Y., Kwan, K., Diver, R., Siegal, N., Weimer, A., Perkins, C., Lewandowski, A., 2010. High efficiency generation of hydrogen fuels using solar thermal-chemical splitting of water (Solar Thermo-Chemical Splitting for H2), Las Vegas.
Miller, J.E., Evans, L.R., Stuecker, J.N., Allendorf, M.D., Siegel, N.P., Diver, R.B., 2006. Materials development for the CR5 solar thermochemical heat engine. In: ASME 2006 International Solar Energy Conference. pp. 311–320. Available at: <http://dx.doi.org/10.1115/ISEC2006-99152>.
Miller, J.E., Allendorf, M.D., Diver, R.B., Evans, L.R., Siegel, N.P., Stuecker, J.N., 2008. Metal oxide composites and structures for ultra-high temperature solar thermochemical cycles. J. Mater. Sci. 43 (14), 4714–4728.
Miller, J.E., Allendorf, M.D., Ambrosini, A., Chen, K., Coker, E.N., Dedrick, D.E., Diver, R.B., Hogan, R.E., Ermanoski, I., Johnson, T.A., Kellogg, G.L., McDaniel, A.H., Siegel, N.P., Staiger, C.L., Stechel, E.B., 2012. Final Report. Reimagining Liquid Transportation Fuels: Sunshine to Petrol (Sandia report). Sandia National Laboratories, Albuquerque, NM.
Nakakura, M., Ohtake, M., Matsubara, K., Yoshida, K., Cho, H.S., Kodama, T., Gokon, N., 2015. Development of a receiver evaluation system using 30 kW_{th} point concentration solar simulator. Energy Procedia 69, 497–505.
Neises, M., Roeb, M., Schmücker, M., Sattler, C., Pitz-Paal, R., 2009. Kinetic investigations of the hydrogen production step of a thermochemical cycle using mixed iron oxides coated on ceramic substrates. Int. J. Energy Res. 34 (8), 651–661. Available at: http://doi.wiley.com/10.1002/er.1565.
OSRAM, 2006. XBO 6000W/HSLA OFR Technical Information No. 5395 Theater Lamps. Technology and Application.
OSRAM, 2008. XBO – Theater Lamps. Technology and Application.
Pagkoura, C., Karagiannakis, G., Zygogianni, A., Lorentzou, S., Konstandopoulos, A.G., 2015. Cobalt oxide based honeycombs as reactors/heat exchangers for redox thermochemical heat storage in future CSP plants. Energy Procedia 69, 978–987. Available at: http://linkinghub.elsevier.com/retrieve/pii/S1876610215004890.
Palumbo, R.D., Fletcher, E.A., 1988. High temperature solar electrothermal processing-III. Zinc from zinc oxide at 1200–1675 K using a non-consumable anode. Energy 13 (4), 319–332.
Perkins, C., Weimer, A.W., 2004. Likely near-term solar-thermal water splitting technologies. Int. J. Hydrogen Energy 29, 1587–1599.
Petrasch, J., Coray, P., Meier, A., Brack, M., Häberling, P., Wuillemin, D., Steinfeld, A., 2006. A novel 50 kW 11,000 suns high-flux solar simulator based on an array of xenon arc lamps. J. Sol.Energy Eng. 129 (4), 405–411. Available at: http://dx.doi.org/10.1115/1.2769701.
Roeb, M., Monnerie, N., Schmitz, M., Sattler, C., Konstandopoulos, A.G., Agrafiotis, C. C., Zaspalis, V.T., Nalbandian, L., Steele, A.M., Stobbe, P., 2006. Thermo-chemical production of hydrogen from water by metal oxides fixed on ceramic substrates. In: Proceedings of the 16th World Hydrogen Energy Conference, Lyon, France, June, WHEC 16, pp. 1–12.
Roeb, M., Säck, J.P., Rietbrock, P., Prahl, C., Schreiber, H., Neises, M., de Oliveira, L., Graf, D., Ebert, M., Reinalter, W., Meyer-Grünefeldt, M., Sattler, C., Lopez, A., Vidal, A., Elsberg, A., Stobbe, P., Jones, D., Steele, A., Lorentzou, S., Pagkoura, C., Zygogianni, A., Agrafiotis, C., Konstandopoulos, A.G., 2011. Test operation of a 100 kW pilot plant for solar hydrogen production from water on a solar tower. Sol. Energy 85 (4), 634–644. Available at: http://dx.doi.org/10.1016/j.solener.2010.04.014.
Säck, J.P., Breuer, S., Cotelli, P., Houaijia, A., Lange, M., Wullenkord, M., Spenke, C., Roeb, M., Sattler, C., 2016. High temperature hydrogen production: design of a 750 kW demonstration plant for a two-step thermochemical cycle. Sol. Energy 135, 232–241. Available at: http://linkinghub.elsevier.com/retrieve/pii/S0038092X16301773.
Sarwar, J., Georgakis, G., LaChance, R., Ozalp, N., 2014. Description and characterization of an adjustable flux solar simulator for solar thermal, thermochemical and photovoltaic applications. Sol. Energy 100, 179–194. Available at: http://www.sciencedirect.com/science/article/pii/S0038092X13005252.
Scheffe, J.R., Li, J., Weimer, A.W., 2010. A spinel ferrite/hercynite water-splitting redox cycle. Int. J. Hydrogen Energy 35 (8), 3333–3340.
Schwartzwalder, K., Somers, A.V., 1963. Method of making porous ceramic articles. US Pat. No. 3090094, May 21.
Steinfeld, A., 2005. Solar thermochemical production of hydrogen – a review. Sol. Energy 78, 603–615.
Walker, L.S., Miller, J.E., Hilmas, G.E., Evans, L.R., Corral, E.L., 2012. Coextrusion of zirconia-iron oxide honeycomb substrates for solar-based thermochemical generation of carbon monoxide for renewable fuels. Energy Fuels 26 (1), 712–721.
Wang, W., Aichmayer, L., Laumert, B., Fransson, T., 2014. Design and validation of a low-cost high-flux solar simulator using fresnel lens concentrators. Energy Procedia 49, 2221–2230.